Icarus 251 (2015) 65–95

Contents lists available at ScienceDirect

Icarus

journal homepage: www.elsevier.com/locate/icarus

Eight-year climatology of dust optical depth on Mars

L. Montabone [a,b,c,*], F. Forget [a], E. Millour [a], R.J. Wilson [d], S.R. Lewis [e], B. Cantor [f], D. Kass [g], A. Kleinböhl [g], M.T. Lemmon [h], M.D. Smith [i], M.J. Wolff [c]

[a] Laboratoire de Météorologie Dynamique, Université Pierre et Marie Curie, Paris, France
[b] Department of Physics, University of Oxford, Oxford, UK
[c] Space Science Institute, Boulder, CO 80301, USA
[d] NOAA/GFDL, Princeton, NJ 08540-6649, USA
[e] Department of Physical Sciences, The Open University, UK
[f] Malin Space Science Systems, San Diego, CA 92121, USA
[g] JPL, Pasadena, CA 91109, USA
[h] Texas A&M University, College Station, TX 77843, USA
[i] NASA Goddard Space Flight Center, Greenbelt, MD 20771, USA

ARTICLE INFO

Article history:
Received 9 March 2014
Revised 18 November 2014
Accepted 31 December 2014
Available online 2 February 2015

Keyword:
Mars, atmosphere
Mars, climate
Data reduction techniques

ABSTRACT

We have produced a multiannual climatology of airborne dust from martian year 24–31 using multiple datasets of retrieved or estimated column optical depths. The datasets are based on observations of the martian atmosphere from April 1999 to July 2013 made by different orbiting instruments: the Thermal Emission Spectrometer (TES) aboard Mars Global Surveyor, the Thermal Emission Imaging System (THEMIS) aboard Mars Odyssey, and the Mars Climate Sounder (MCS) aboard Mars Reconnaissance Orbiter (MRO). The procedure we have adopted consists of gridding the available retrievals of column dust optical depth (CDOD) from TES and THEMIS nadir observations, as well as the estimates of this quantity from MCS limb observations. Our gridding method calculates averages and uncertainties on a regularly spaced spatio-temporal grid, using an iterative procedure that is weighted in space, time, and retrieval quality. The lack of observations at certain times and locations introduces missing grid points in the maps, which therefore may result in irregularly gridded (i.e. incomplete) fields. In order to evaluate the strengths and weaknesses of the resulting gridded maps, we compare with independent observations of CDOD by Pan-Cam cameras and Mini-TES spectrometers aboard the Mars Exploration Rovers "Spirit" and "Opportunity", by the Surface Stereo Imager aboard the Phoenix lander, and by the Compact Reconnaissance Imaging Spectrometer for Mars aboard MRO. We have statistically analyzed the irregularly gridded maps to provide an overview of the dust climatology on Mars over eight years, specifically in relation to its interseasonal and interannual variability, in addition to provide a basis for instrument intercomparison. Finally, we have produced regularly gridded maps of CDOD by spatially interpolating the irregularly gridded maps using a kriging method. These complete maps are used as dust scenarios in the Mars Climate Database (MCD) version 5, and are useful in many modeling applications. The two datasets for the eight available martian years are publicly available and distributed with open access on the MCD website.

1. Introduction

The dust cycle is currently considered to be the key process controlling the variability of the martian climate at seasonal and interannual time scales, as well as the weather variability at much shorter time scales. The atmospheric thermal and dynamical structures, and the transport of aerosols and chemical species, are all strongly dependent on the dust spatio-temporal distribution, particle sizes, and optical properties.

After the first systematic observations of a planet-encircling dust storm by ground-based telescopes in the late 1950s, the study of dust has been one of the main objectives of many spacecraft missions to Mars over more than 40 years. Recent and ongoing missions, such as Mars Global Surveyor (MGS), Mars Odyssey (ODY), Mars Express, Mars Exploration Rover (MER), Mars Reconnaissance Orbiter (MRO), Phoenix, and Mars Science Laboratory, have included spectrometers, radiometers, imagers, cameras, and

* Corresponding author at: Laboratoire de Météorologie Dynamique, Université Pierre et Marie Curie, Tour 45-55, 3ème étage, 4, place Jussieu, F 75252 Paris Cedex 05, France.
E-mail address: lmontabone@SpaceScience.org (L. Montabone).

http://dx.doi.org/10.1016/j.icarus.2014.12.034
0019-1035/

one LIDAR to measure radiances at wavelengths sensitive to dust. See Smith (2008) for an extensive review of spacecraft instruments sensitive to dust prior to the Surface Stereo Imager (SSI) and the LIDAR aboard the Phoenix lander (Smith et al., 2008), and the Mastcam camera aboard the Mars Science Laboratory rover (Grotzinger et al., 2012).

One of the key physical parameters used to quantify the presence and spatial distribution of mineral dust in the atmosphere is the vertically-integrated, or column, optical depth (also called optical thickness). It is related to how much radiation at a specific wavelength would be removed from the vertical component of a beam during its path through the atmosphere by absorption and scattering (i.e. extinction) due to airborne dust. The column optical depth is the product of dust retrievals when the radiance observations are obtained by nadir-viewing instruments. Vertical profiles of extinction opacity (or extinction coefficient) can be derived from radiances measured by limb-viewing instruments, providing important information on the vertical extension of the dust. Although relative variations of optical depth can be readily obtained from remote observations, absolute values are much trickier to obtain because they require accurate knowledge of important properties related to dust, such as the particle size distribution and the optical parameters. These properties are difficult to retrieve from direct measurements of radiances (Clancy et al., 2003; Wolff and Clancy, 2003; Wolff et al., 2006, 2009).

Dust climatology is a terminology generally adopted to indicate dust data (e.g. observed horizontal and vertical distributions) that characterize specific times and locations, but can be assumed as valid at other times and locations in a statistical sense. Because there are relatively few observations of dust on Mars, which do not cover all times and locations, the use of dust climatologies as "dust scenarios" is common practice in modeling studies of the martian atmosphere. Dust climatologies are also commonly used as input values for atmospheric species and surface quantity retrievals, e.g. atmospheric ozone (Clancy et al., 2014), surface albedo (Vincendon et al., 2014), and surface thermal inertia (Putzig and Mellon, 2007), to cite only a few.

The choice of dust scenarios has a significant impact on martian model simulations. The knowledge of the dust spatio-temporal distribution is essential to produce quantitative estimates of dust mass mixing ratios, and calculate the atmospheric heating rates due to absorption and scattering of solar and infrared (IR) radiation by airborne particles. These calculations are the basis for describing the thermal forcing in Mars atmospheric models, such as global climate models (GCM), and producing accurate predictions of the atmospheric state. Model studies have often been carried out with analytical specifications of dust distributions, both in the horizontal and in the vertical (see e.g. Forget et al., 1999; Montmessin et al., 2004; Kuroda et al., 2008). More recently, modeling groups have been carrying out simulations with more realistic horizontal dust distributions, tied to TES observations. A non-exhaustive list of examples includes Guzewich et al. (2013a), Wang and Richardson (2015), Kavulich et al. (2013), Greybush et al. (2012), Madeleine et al. (2011, 2012). Steele et al. (2014b) use an horizontal dust distribution derived from MCS observations in martian year (MY) 30, which is an early version of the MY 30 dust scenario presented in this paper.

We propose in this paper to create a well-documented, multiannual, 2D dust climatology of the column dust optical depth (CDOD), as well as a set of dust scenarios to be used in model experiments. Although we focus our attention on the column-integrated dust distribution, it should be noted that the spatial variation of the vertical distribution of dust also plays a significant role in thermal response (see e.g. Guzewich et al., 2013a). There are a number of approaches to represent this vertical structure (e.g. Madeleine et al., 2011; Greybush et al., 2012), all of which are based on the constraint of observed dust optical depths.

To date, there exist several datasets of retrieved CDOD for Mars, spanning more than 20 martian years since the Mariner era (e.g. Fenton et al., 1997). These datasets are highly heterogeneous, as they have been created using data from different instruments having different geometric views, spatial and temporal coverage, as well as different observing wavelengths. Nonetheless, we show in this paper that at least some of these datasets can be appropriately used to quantitatively reconstruct the recent dust climatology on Mars, and characterize the variability over many seasonal cycles. This paper seeks to produce a continuous, multiannual climatology of CDOD from early March 1999 (solar longitude $L_s \sim 104^\circ$ in MY 24) to the end of July 2013 ($L_s = 360^\circ$ in MY 31). During this period of time, the Thermal Emission Spectrometer (TES, Christensen et al., 2001) aboard MGS, the Thermal Emission Imaging System (THEMIS, Christensen et al., 2004) on ODY, and the Mars Climate Sounder (MCS, McCleese et al., 2007) on MRO provided global coverage of radiance observations at IR wavelengths, from which Smith et al. (2003), Smith (2004, 2009), Kleinböhl et al. (2009) obtained direct retrievals of CDOD or estimates of this quantity from the integrated extinction profiles.

While images from orbiting spacecraft can provide information over large areas on the planet at any given time, observations of IR radiances from orbiting instruments have a very discrete coverage in longitude and local time due to the choice of orbit geometry. MGS and MRO, for instance, have Sun-synchronous, nearly 2-h polar orbits, which provide good latitude coverage but only sample about a dozen longitudes per day, usually at close to two fixed local times except when crossing the poles. Because dust storms on Mars have a wide range of spatial and temporal scales (Cantor, 2007; Wang et al., 2003, 2005), these discrete observations can affect the space–time representation of dust storm activity. Extrapolating the data collected along orbit tracks to a broader range of local time and longitude introduces even more biases. Global maps produced using simple average binning may alter the representation of rapidly evolving dust distribution.

We have developed a gridding methodology that is specifically adapted to heterogeneous observations, and to the discrete longitudinal/temporal coverage typical of spacecraft data acquisition. The ultimate objective is to produce regularly gridded maps of absorption CDOD at 9.3 μm for several consecutive martian years (dust optical depth in absorption is less dependent on the particle size than in extinction). To achieve this goal, we have adopted a two-step procedure. The first step consists in iteratively calculating averages of observations and related uncertainties on a regularly spaced spatio-temporal grid, after having binned the data using time windows of different size, and applied appropriate weighting functions in space, time, and retrieval quality at each iteration. The lack of observations at certain times and locations introduces missing grid points in the maps, which are therefore likely to result as incomplete, or irregularly gridded. We have used this first product to statistically study the dust variability over almost eight complete martian years. The second step consists in producing regular maps of CDOD by spatially interpolating and/or extrapolating the irregularly gridded maps, using a kriging method (see e.g. Journel and Huijbregts, 1978, for a general introduction on the technique). This multiannual series of complete maps of CDOD is used for the dust scenarios in the GCM simulations that produce the current version of the Mars Climate Database (MCD version 5, Millour et al., 2014).

We provide open access to both the irregularly gridded and regularly kriged datasets, to foster scientific analyses and applications of the long-term martian dust climatology. The most up-to-date version of these products (currently v2.0) can be downloaded in

the form of NetCDF files from the MCD project website,[1] hosted by the Laboratoire de Météorologie Dynamique (LMD) in Paris, France. We also provide animations of the multiannual products as supplementary material to this publication. These quantitative datasets have a qualitative counterpart in the multiannual visible dust climatology dataset described in Wang and Richardson (2015), based on images taken by the Mars Orbiter Camera (MOC) aboard MGS and the Mars Color Imager (MARCI) aboard MRO.[2]

The outline of this paper is the following. Section 2 describes the instruments and data we have used to produce the dust climatology. We provide details of the time coverage, data quality control, processing, and uncertainties. In Section 3 we introduce the iterative weighted binning methodology we have adopted to create irregularly gridded CDOD maps from the spacecraft observations. Section 4 is devoted to the discussion of the internal validation of the gridded maps, as well as their validation with independent observations. We report in Section 5 on the statistical analysis of the dust climatology, in relation to the interseasonal and interannual variabilities. In Section 6 we discuss the assumptions we have made and the kriging technique we have applied, with the purpose of producing regularly gridded (i.e. complete) maps to be used as dust scenarios. A summary is outlined in Section 7, including a discussion on future developments.

2. Spacecraft, instruments and observations

Mars Global Surveyor started its science mapping phase in March 1999 ($L_s \sim 104^\circ$, MY 24), after a lengthy period of aerobraking during which its orbit was very elliptical (with orbit period much longer than the nominal 2-h mapping phase orbit). MGS stopped working properly in November 2006, and the mission was officially ended in January 2007. Mars Odyssey started its mapping phase in February 2002 ($L_s \sim 330^\circ$, MY 25) and is still currently working (as of October 2014). It is the longest running spacecraft orbiting an extra-terrestrial planet to date. Mars Reconnaissance Orbiter started its mapping phase in November 2006 ($L_s \sim 128^\circ$, MY 28) and, although it encountered a few problems that kept it in safe mode for an extended period at the end of 2009, is operating nominally at the time of writing. The Mars Exploration Rovers "Spirit" and "Opportunity" started their missions on Mars respectively on January 4, 2004 ($L_s \sim 328^\circ$, MY 26) in Gusev crater, and January 25, 2004 in Meridiani Planum ($L_s \sim 339^\circ$, MY 26). Spirit ceased communications with Earth in March 2010 ($L_s \sim 67^\circ$, MY 30), whereas Opportunity is still active on the surface of the planet (as of October 2014). The Phoenix lander started its short mission in the so-called "Green Valley" site within Vastitas Borealis on May 25, 2008 ($L_s \sim 76^\circ$, MY 29), and officially ended it on November 10, 2008 ($L_s \sim 155^\circ$, MY 29).

For the purpose of building the dust climatology described in this paper, we have used CDOD retrievals and estimates obtained from the following instruments observing at IR wavelengths:

- TES aboard MGS, from $L_s = 103.6^\circ$ in MY 24 to $L_s = 82.5^\circ$ in MY 27. After this date, the number and quality of TES observations rapidly decreased (August 2004). Absorption CDODs (scattering is not modeled) are retrieved from nadir observations, and values reported at a reference wavelength of 1075 cm^{-1}, or 9.3 μm (Smith, 2004). Local times are narrowly centered around 14:00 h at most latitudes, except when the orbit crosses high latitudes.
- THEMIS aboard ODY, from $L_s = 0^\circ$ in MY 26 (we did not use observations taken at the end of MY 25) to $L_s = 360^\circ$ in MY 31 (observations are still available after this date). Absorption CDODs are retrieved from nadir observations, and values reported at a reference wavelengths of 1075 cm^{-1}, or 9.3 μm, as for TES (Smith et al., 2003; Smith, 2009). Local times are between 14:30 and 18:00 h at most latitudes equatorward of ±60°.
- MCS aboard MRO, from $L_s = 111.3^\circ$ in MY 28 to $L_s = 360^\circ$ in MY 31 (observations are still available after this date). MCS was switched on in September 2006 before the official beginning of MRO primary science phase, but had a long period in MY 28 (between February 9 and June 14, 2007) during which a mechanical problem preventing the use of its elevation actuator forced the team to keep it in limb-staring mode. The event precluded any nadir or off-nadir observation during this period, with the effect of limiting the vertical extension of the retrieved profiles – including those of extinction opacity – in the lower part of the atmosphere. Since October 9, 2007, off-nadir measurements with surface incidence angles between about 60° and 70° have resumed with nearly every limb sequence, but for retrievals of aerosol extinction opacities only limb views are currently used. Kleinböhl et al. (2009) obtained profiles of dust extinction opacity from limb observations at wavelengths centered around 463 cm^{-1} (21.6 μm) as standard MCS product. In this paper we have used estimates of CDOD from the limb observations, as described in Section 2.1.2. Local times are centered around 03:00 and 15:00 h at most latitudes, except when the orbit crosses the polar regions. Since September 13, 2010 ($L_s = 146^\circ$, MY 30) MCS has also been able to observe cross-track, thus providing information in a range of local times at selected positions during the MRO orbits (Kleinböhl et al., 2013). We include these cross-track observations in our gridding, when available.

For the purpose of validating the gridded maps with independent observations, we have used retrievals of near-IR and IR CDOD from the following instruments:

- PanCam cameras (Bell et al., 2003) aboard MER-A "Spirit" and MER-B "Opportunity", respectively from $L_s \sim 328^\circ$ and $L_s \sim 339^\circ$ in MY 26. Spirit PanCam stopped providing measurements after $L_s \sim 67^\circ$ in MY 30. Lemmon et al. (2015) have retrieved CDOD from upward-looking observations at wavelengths centered around 880 nm (near IR) and 440 nm (visible blue). In this work we use only retrievals at 880 nm. There are no significant differences between the values provided at the two wavelengths.
- Mini-TES (Christensen et al., 2003) aboard MER "Spirit" and "Opportunity", starting from the same times as PanCam cameras until $L_s \sim 191^\circ$ (Spirit) and $L_s \sim 269^\circ$ (Opportunity) in MY 28. After $L_s \sim 269^\circ$ the detectors were covered by dust from the MY 28 planet-encircling dust storm and became unreliable. Smith et al. (2006) have retrieved CDOD from upward-looking observations at IR wavelengths centered around 1075 cm^{-1} (9.3 μm).
- CRISM (Murchie et al., 2007) aboard MRO, from $L_s \sim 133^\circ$ in MY 28 until $L_s = 360^\circ$ in MY 30. CDOD retrievals have been obtained from nadir observations at wavelengths centered around 900 nm (Wolff et al., 2009). Although there are CRISM observations available after $L_s = 360^\circ$ in MY 30, we do not use these observations in the present work because an issue of truncated EPFs in MY 31 requires further investigation.
- SSI (Smith et al., 2008) aboard Phoenix lander, from $L_s = 78.0^\circ$ until $L_s = 148.6^\circ$ in MY 29. Lemmon et al. (2008) have retrieved CDOD from upward-looking observations at wavelengths centered around 887 nm (near-IR).

[1] The URL to access the website is: http://www-mars.lmd.jussieu.fr/.

[2] See also regular weather reports for MOC at http://www.msss.com/mars_images/moc/weather_reports/ and for MARCI at http://www.msss.com/msss_images/latest_weather.html.

Fig. 1 shows a summary of the time periods for which observations from the above mentioned instruments are available, together with the time limits within which we have used them in this paper.

In addition to CDOD data, we have also used visible wide-angle images from MGS/MOC (Malin et al., 2010), and visible images from MRO/MARCI (Bell et al., 2009). The main purpose is to compare the evolution of selected dust storms in the reconstructed CDOD maps to the evolution that can be appreciated in high-resolution camera images of the martian surface.

2.1. Data quality control

Before using the CDOD retrievals from the different instruments, we have checked the values against quality control criteria to eliminate unreliable data.

For all datasets, negative values are only allowed if the sum of the value and the associated uncertainty (see Section 2.3) is non-negative. Although a single negative measurement – in this specific case a 'measurement' corresponds to a 'retrieval' – can be considered unphysical, the weight of negative measurements must be taken into account in statistical calculations to prevent biases towards large opacity values. It is anticipated that both the gridded values described in Section 3 and the interpolated ones described in Section 6 are only accepted if they are positive, otherwise they are replaced by a minimum positive value of 0.01 (IR absorption CDOD at 9.3 μm), which is compatible with the background noise.

For specific datasets, we have considered the quality control criteria described below. We show in Figs. 2 and 3 the number of CDOD retrievals used in the present work, as a function of year, latitude, and season.

2.1.1. TES and THEMIS

For TES, we have retained CDOD observations that are flagged as "good quality" by the TES team in the NASA Planetary Data System release, and have passed additional quality control criteria. Specifically, we require that the surface temperature is greater than 220 K (Smith, 2004), the difference between surface temperature and atmospheric temperature at the lowest available pressure level is greater than 5 K, the radiance fit residual is lower than 20, the opacity of the carbon dioxide hot bands is between −0.01 and 0.05, and the water ice opacity is greater than −0.05 (the negative value threshold is constrained by the uncertainty). The surface temperature threshold ensures a good signal-to-noise ratio, whereas the threshold on the temperature difference between surface and atmosphere prevents unreliable retrievals when the temperature contrast is too small. The latter case is particularly valid during high dust loading conditions, as showed by results from the Geophysical Fluid Dynamics Laboratory GCM (GFDL-GCM) and comparison with MOC images during the 2001 planet-encircling dust storm (Wilson et al., 2008). With this choice of quality control criteria, retrievals are effectively limited to daytime conditions over ice-free surfaces, and their number may be reduced during intense dust storms, and at the edge of the polar night (see Figs. 2 and 3). Future versions of the gridded maps could benefit from the introduction of recently retrieved nightside TES CDODs (Pankine et al., 2013).

THEMIS CDOD retrievals include several "framelets" in the same "image", i.e. several values within the same stripe of observations. Only the last framelet of each image is properly calibrated, but in this study we have considered all available framelets to increase the number of THEMIS observations, especially in MY 27 after $L_s = 82.5^\circ$ when we use no other observations. We associate a slightly larger uncertainty with non-calibrated framelets, as explained in Section 2.3. For quality control purposes, we have retained CDOD values when the rms residual from the aerosol opacity fit is lower than 0.4, and the surface temperature is greater than 210 K.

2.1.2. MCS

MCS observes the atmosphere in limb and off-nadir modes, which has the advantage of allowing the retrieval of vertical profiles of temperature and aerosols, but has the disadvantage of not being able to observe the first few kilometres above the ground (depending on the angle of observation). In order to estimate the column optical depth for aerosol dust, the MCS team has integrated the full profile of dust extinction opacity produced by the retrieval algorithm – we use version v4.3 in this work – during a successful limb retrieval. The profile is extended upward and downward under the assumption of well mixed dust, based on the last valid value. The standard retrieved dust profile is often truncated when regions have measured radiances that are not fit by the forward radiative model within defined thresholds in dust, water ice or temperature. In the upper levels, the minimum extinction coefficient threshold for dust is 10^{-9} km^{-1}. At the lower levels, the profiles can become saturated by high opacity values, exceeding the threshold of 10^{-3} km^{-1} (Kleinböhl et al., 2009). Column optical depth estimates, on the other hand, use non-truncated profiles to make sure all available and reasonable information is taken into account. The MCS dust profiles cannot be retrieved down to the surface using only limb observations, and the dust in the

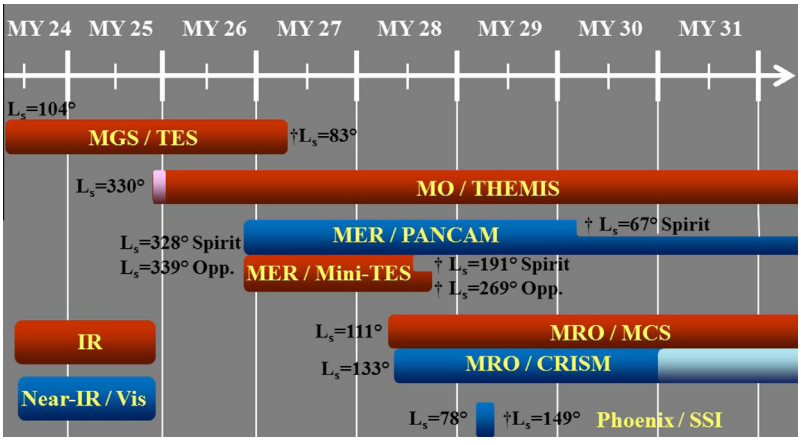

Fig. 1. A summary of the time coverage of all instruments used in this work, and the time limits within which observations are available. Lighter colors in the bars indicate the periods when observations from that particular instrument are available but either there are no CDOD retrievals available or we do not currently use them. (For interpretation of the references to color in this figure legend, the reader is referred to the web version of this article.)

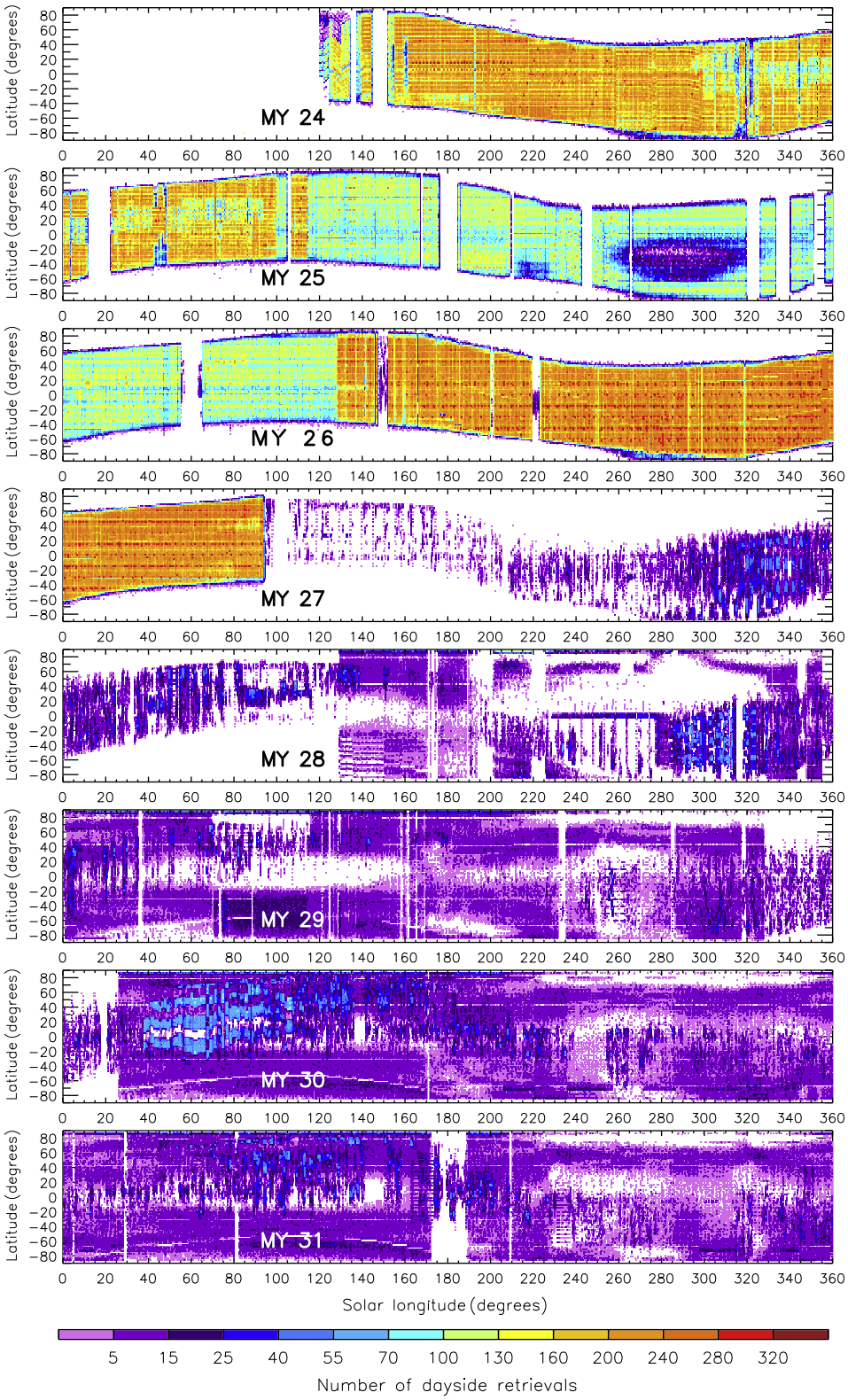

Fig. 2. The number of dayside retrievals of column dust optical depth (local times between 06:00 and 18:00) passing the quality control procedure described in the text. The number of retrievals is summed in 1 sol × 2° latitude bins, and plotted for each year as a function of solar longitude and latitude. TES observed at higher spectral resolution (5 cm^{-1}) between $L_s \sim 115°$ in MY 25 and $L_s \sim 128°$ in MY 26, therefore there are considerably fewer observations in this period, because the high spectral resolution data take twice as long to acquire as the low spectral resolution. Note that THEMIS retrievals are summed together with TES retrievals and MCS retrievals, when available.

un-retrieved part of the profile can account for a significant fraction of the total dust column. Estimates of CDOD from MCS observations, therefore, are likely to introduce errors attributable to either the extrapolation to the surface under the well mixed assumption or the use of dust opacity values at altitudes where the fit to observed radiances is not within the standard threshold. This problem may be particularly acute in light of evidence of elevated dust layers (Heavens et al., 2011; Guzewich et al., 2013b).

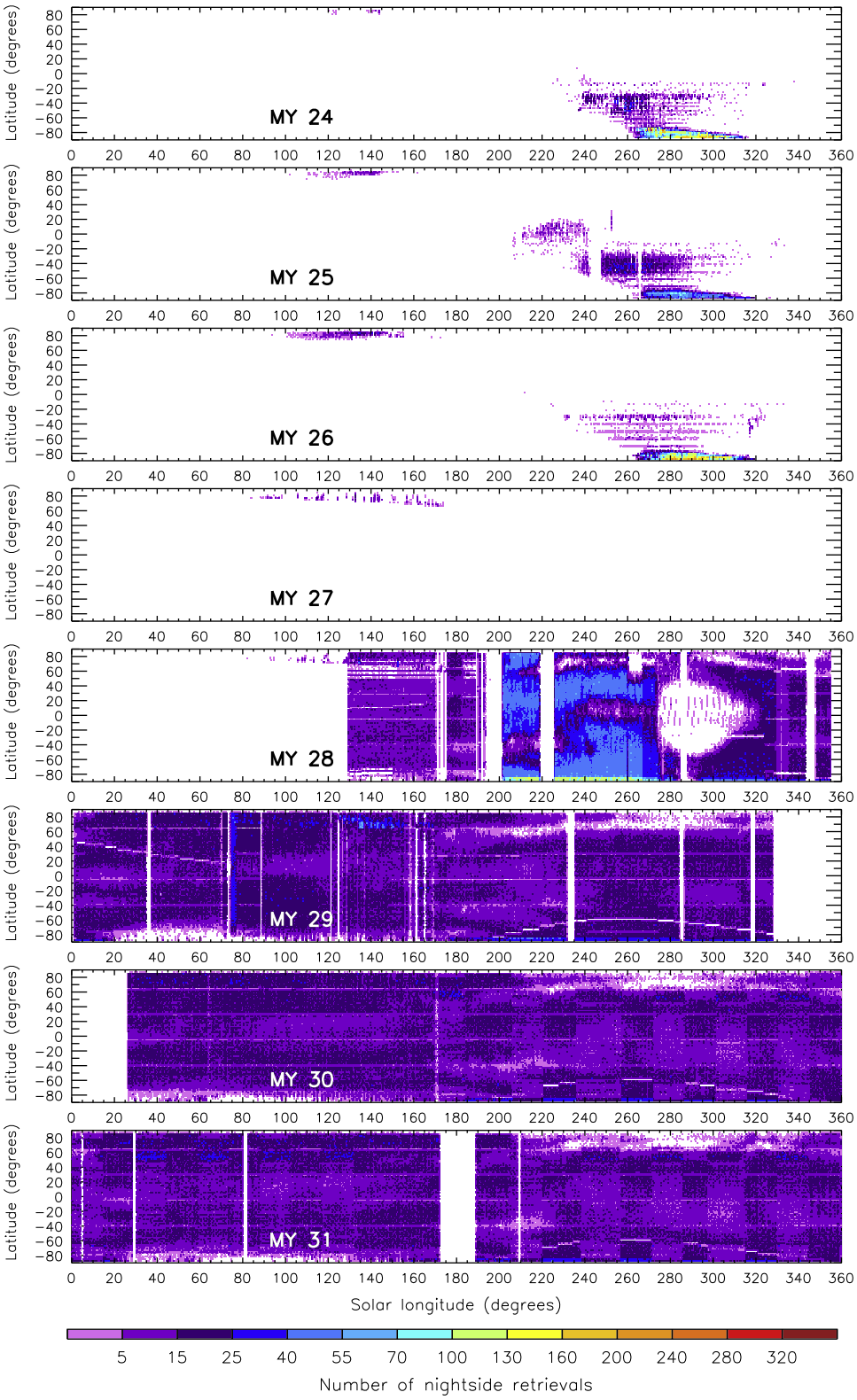

Fig. 3. As for Fig. 2, but for nightside retrievals, with local times between 00:00 and 06:00, and between 18:00 and 24:00.

MCS CDOD estimates can be fairly inaccurate if the lowest retrieved level of dust opacity is above ~20 km altitude, depending on the time of the year and the dust/water ice conditions. Dayside estimates are particularly affected by low altitude aerosols, e.g. water ice clouds. We have therefore retained nighttime CDODs that correspond to dust extinction profiles with valid values at or below 25 km altitude, and we only accept CDODs with local times between 12:00 and 18:00 h when the corresponding extinction profile has valid values at or below 8 km altitude. The use of different altitude thresholds for nighttime and most daytime CDODs is particularly important when spurious diurnal variability could be introduced by large extrapolation of dust extinction coefficient to

the surface during afternoon observations, at seasons and locations where the water ice component is abundant (Figs. 12 and 13 of McCleese et al., 2010, give an idea of the diurnal variability of the dust extinction profile). It is worth mentioning that this selection might introduce a systematic bias, especially during the northern spring and summer seasons in the tropics. TES provides daytime CDODs while MCS estimates of CDOD in this season are largely based on nighttime viewing, because daytime clouds in the aphelion tropical belt limit the success of the retrievals in altitude. The filtering of dayside CDOD estimates could be refined in future versions of the gridded maps, to avoid biasing towards nightside observations.

Finally, we have rejected CDOD estimates when the temperature profile dropped below the condensation temperature of carbon dioxide at some pressure levels, because CO_2 ice opacity can affect retrievals of dust opacity at those levels (carbon dioxide ice opacity is not currently taken into account in MCS retrievals v4.3).

2.2. Data processing

The CDODs from TES/THEMIS and MCS are retrieved at different IR wavelengths (in absorption for TES/THEMIS and in extinction for MCS), which prevents the direct comparison. We account for this by converting the estimated MCS extinction CDODs at 21.6 μm into equivalent absorption CDODs at 9.3 μm. We carry out the conversion by multiplying the MCS values by a factor 2.7 (according to Kleinböhl et al., 2009, 2011), which takes into account the effective dust particle radius (1.06 μm) and variance (0.3) used in the retrievals v4.3. It is worth mentioning that the assumed dust size distribution remains fixed for all seasons and locations. This factor is affected by an estimated uncertainty of 10%, which we apply to MCS data as explained in Section 2.3.2.

In order to calculate spatial averages, we require that each retrieved CDOD be normalized to a reference pressure level to eliminate the effect of topographic inhomogeneities. Each value is therefore divided by the surface pressure at the appropriate location, local time, and season, which is extracted from the PRESO tool included in the MCD v4.3 (Millour et al., 2011), and multiplied by 610 Pa (our choice for the reference pressure level). This is equivalent to integrating or extrapolating the optical depth to 610 Pa at all locations on the planet, under the assumption of well-mixed dust. See also Section 2.3 for a discussion of uncertainties associated with surface pressure. The following formulas summarize the processing of CDOD observations:

$$\mathrm{CDOD610}_{\mathrm{absIR9.3}} = \begin{cases} (\mathrm{CDOD}_{\mathrm{absIR9.3}}/P_s)*610 & \text{for TES/THEMIS} \quad \text{(a)} \\ [(\mathrm{CDOD}_{\mathrm{extIR21.6}}*2.7)/P_s]*610 & \text{for MCS} \quad \text{(b)} \end{cases} \quad (1)$$

where P_s is the surface pressure. Although our emphasis is on normalized CDODs (CDOD610), our gridded and kriged products also include full column (or total) optical depths, obtained with the procedure described in Appendix B.

Finally, when using PanCam, SSI, and CRISM for validating the gridded maps in Section 4, we have to account for the differences between the IR absorption-only gridded values and the full extinction near-IR observations (CDODs from PanCam cameras are provided at the 880 nm wavelength, from SSI at the 887 nm wavelength, and from CRISM at the 900 nm wavelength). This is done by converting PanCam, SSI, and CRISM CDODs into equivalent IR absorption CDODs. The process firstly converts values from visible (or near-IR) to full-extinction IR by dividing by a factor 2.0, consistent with 1.5- to 2.0-μm dust particle radii (Clancy et al., 2003; Lemmon et al., 2004; Wolff et al., 2006; Lemmon et al., 2015). Secondly, it converts full-extinction IR values to absorption-only at 9.3 μm by dividing by a factor 1.3 (Smith, 2004; Wolff and Clancy, 2003). Overall, the factor we divide by to convert from full-extinction near-IR to equivalent absorption-only at 9.3 μm is 2.6. This factor, though, is affected by large errors, deriving from both the visible-to-infrared conversion (Lemmon et al., 2004; Wolff et al., 2006; Lemmon et al., 2015) and the conversion to absorption (Smith, 2004), see Section 2.3.4 for more details. This is the reason why we have decided to provide our gridded products at the original IR wavelengths, despite the advantage of producing equivalent visible CDOD maps for global and mesoscale atmospheric models. Their radiation schemes, in fact, usually compute dust heating rates based on mean visible opacities, using assumed IR/visible ratios. PanCam, SSI, and CRISM observations are also normalized to 610 Pa when they are compared to the gridded values in Section 4.

2.3. Data uncertainties

We have estimated the uncertainties of each single CDOD observation and CDOD610 value that we have used in this work. The combined standard uncertainty of a CDOD610 value is calculated as the propagation of uncertainties on CDOD, surface pressure, and the 2.7 factor, according to Eq. (1). The error propagation is carried out using relative errors, which highly simplify the formulas. The squared relative propagated error reduces to the sum of the squared relative errors of each independent variable when operations among variables include only multiplications and divisions, as in our case.

A surface pressure value extracted from the MCD v4.3 has an associated uncertainty. The corrections for high resolution topography and total mass of the atmosphere are carried out within the PRESO routine of the MCD. For the former, the routine uses the 32 pixels/degree MGS/MOLA topography, which is equivalent to less than 2 km resolution in longitude and latitude at the equator. The topography resolution is therefore comparable to the footprint size of the TES instrument (3×8 km). In order to correct for the seasonally varying total mass of the atmosphere, the routine performs a renormalization of the surface pressure values to the values observed by the Viking landers at the corresponding season. Millour et al. (2011) provides examples of validation of the PRESO routine v4.3 using observations from Viking and Phoenix landers. After the topography and total mass corrections, the largest source of surface pressure variability on Mars is related to the weather systems, mainly in the form of dust storms and high latitude winter baroclinic waves. In order to account for this variability, we extracted the day-to-day root mean squared of surface pressure from the MCD (see the MCD Detailed Design Document associated with the version of the database described in Millour et al. (2011)) to build a 5° solar longitude $\times$5° latitude array. We provide an estimate of the surface pressure uncertainty associated with the specific location and season of an observation by interpolating this array. Overall, the surface pressure uncertainty is always less than 3%, with the highest values associated with latitudes and seasons where baroclinic wave activity is strong.

The uncertainties associated with the CDOD for specific instruments are described below.

2.3.1. TES and THEMIS

Retrievals of CDOD from TES and THEMIS observations come with an associated nominal uncertainty, estimated by taking into account random errors in the instrument and calibration, as well as possible systematic errors in the retrieval algorithms. Smith (2004) gives an estimate for the total uncertainty in a single retrieval of TES absorption-only IR dust optical depth: 0.05 or 10% of the column optical depth, whichever is larger. Smith (2009) provides this value for THEMIS absorption-only IR dust optical depth for

the calibrated framelet: 0.04 or 10% of the column optical depth, whichever is larger.

For THEMIS observations, Smith (2009) also states that "uncertainties are likely somewhat higher (perhaps 20% or even higher) during the most intense dust storms because large corrections to the temperature profile must be made for those observations". It is likely that TES retrievals during high dust loading are also affected by larger uncertainties, due to the reduced surface-atmosphere temperature contrast and the uncertainty in the dust size distribution. In order to account for this, for TES we use the nominal uncertainty up to IR optical depth 1.0, then we increase the uncertainty to 20% up to IR optical depth 2.0, and to 30% for IR optical depths greater than 2.0. For THEMIS, we use the nominal uncertainty up to IR optical depth 0.5, we increase the uncertainty to 20% up to IR optical depth 2.0, and to 30% for IR optical depths greater than 2.0.

As for the non-calibrated THEMIS framelets, we currently increase their uncertainties by 20% (e.g. 0.06 instead of 0.05 when the CDOD value is 0.5).

2.3.2. MCS

As explained in Section 2.1, the procedure adopted to estimate CDOD from MCS observations is likely to introduce errors, particularly when the truncated dust profiles do not have valid values close to the surface. Estimating these errors is particularly difficult, as crucial information may be missing in the atmospheric layers where the dust loading is significant. Our estimate of the uncertainty on MCS CDODs, therefore, can only be empirical. In Section 7, we mention future developments in relation to MCS CDOD retrievals.

In this work, we assign a fairly arbitrary uncertainty on the basis of the altitude of the lowest valid level in the dust profile used for the vertical integration. The uncertainty linearly increases from 5% (nominal value) to 60% as a function of this altitude, from the surface to the highest accepted level of 25 km. Although this uncertainty estimate is arbitrary, it provides a way to distinguish MCS values that are likely to be biased, and to relatively evaluate this bias (see also Section 2.4).

Very small values of CDOD estimated from dust extinction profiles that do not have valid values below 4 km are considered spurious and replaced by the minimum value of 0.01, with 10% uncertainty (i.e. 0.001).

Finally, we estimate that the 2.7 factor used to convert MCS extinction CDODs at 21.6 μm to equivalent absorption CDODs at 9.3 μm is affected by 10% uncertainty (i.e. 0.3), due to the uncertainty on the particle sizes. We take this into account in the propagation of uncertainties for MCS.

2.3.3. Other instrument uncertainties

We have averaged CDOD observations from PanCam, Mini-TES, and SSI in each available sol. As a measure of uncertainty on the daily mean, we use the largest value between the standard deviation and the average of single measurement errors. This choice takes into account CDOD variations with local time as well as single measurement errors.

CRISM retrievals are provided with an associated uncertainty, determined from the diagonal of the covariance matrix. Wolff et al. (2009) also indicate a minimum error to handle cases when the formal retrieval error is negligible.

2.3.4. Digression on absorption/extinction and IR/visible conversions

As explained in Section 2.2, we have decided to work at the original TES and THEMIS absorption IR wavelength of 9.3 μm, even when comparing with PanCam, SSI, and CRISM retrievals. The conversion factors from absorption to extinction and from IR to visible depend on the aerosol refractive indexes, which ultimately depend on the aerosol size, shape and composition, and are likely to vary with season and location. Both factors are therefore affected by large uncertainties. Smith (2004) shows in Fig. 4a a graph of the relationship between effective absorption and full extinction optical depth for dust at the equator during the northern autumn equinox in MY 24 (it is stated that the curve is typical of other times and locations). For IR dust optical depths lower than 0.5, the relationship is fairly linear ($\tau_{abs} = \tau_{ext}/1.3$). The departure from the linear relationship at higher dust optical depth can be estimated as $-\tau_{ext}^2/25$. This estimate could be used to introduce an uncertainty on the absorption-to-extinction factor, which increases with the optical depth. As for the infrared-to-visible factor, uncertainties have been estimated in a few measurement campaigns, although limited in time and location. Lemmon et al. (2004) reports a value of 2.0 ± 0.2 from MER-PanCam observations, Wolff et al. (2006) reports in Table 2 dust optical depth values from MER-PanCam and Mini-TES, which can be averaged to provide a value of 2.5 ± 0.6. The most recent work by Lemmon et al. (2015) provides an insight on the interannual and interseasonal variability of this factor at the two MER locations. The average values for Spirit and Opportunity are respectively 2.3 and 2.0, with standard deviations being as large as 0.7 and 0.4.

In Section 4, we have simply used a single factor of 2.6 (i.e. $1.3 * 2.0$) to divide the near-IR extinction values throughout the time series, and convert to equivalent IR absorption values. Nonetheless, we have attempted to take the maximum uncertainty on this factor into account (see Fig. 13).

2.4. Data reliability

As explained in Section 3, our gridding methodology weights the CDOD610 values according to the relative quality of the original CDOD retrievals. The data we use are highly inhomogeneous, as they come from three different instruments, and the retrieval quality generally depends on the amount of aerosols in the atmosphere. Despite the quality control and filtering described in Section 2.1, many observations used in this work have a relatively lower quality, which has to be taken into account when gridding. To this purpose, we associate a reliability value with each single observation, in the range from 1.0 (very reliable) to 0.0 (very unreliable). The reliability value of most CDOD610 observations is simply defined by subtracting the corresponding CDOD relative uncertainty from 1.0, if the relative uncertainty is lower than 1.0. For TES and THEMIS, very low CDOD values have a fixed absolute uncertainty, therefore the relative uncertainties would tend to very large values for small CDODs. In this case, we fix the reliability value to 0.9. THEMIS framelets that are not properly calibrated have reliability values decreased by 0.1, as do very small values of MCS CDOD that do not have valid values below 4 km altitude.

3. Gridding dust optical depth observations

The process of creating uniformly-spaced data (i.e. a regular grid) from irregularly-spaced (scattered) data is generally known as 'gridding'. There exist several techniques to solve this problem, depending on the applications. A basic technique commonly adopted when dealing with orbital spacecraft observations is 'binning' using space–time box averages. The original data values that fall in a given multi-dimensional interval (a 'bin') are replaced by a value representative of that interval – often the average, but the median can also be used to filter outliers. If the bins are uniformly distributed, the problem of gridding the data is solved. For our purposes, the simple box-average binning is not suitable because (1) we seek to achieve the highest possible spatio-temporal resolution for the gridded data, as compatible with having a reasonable

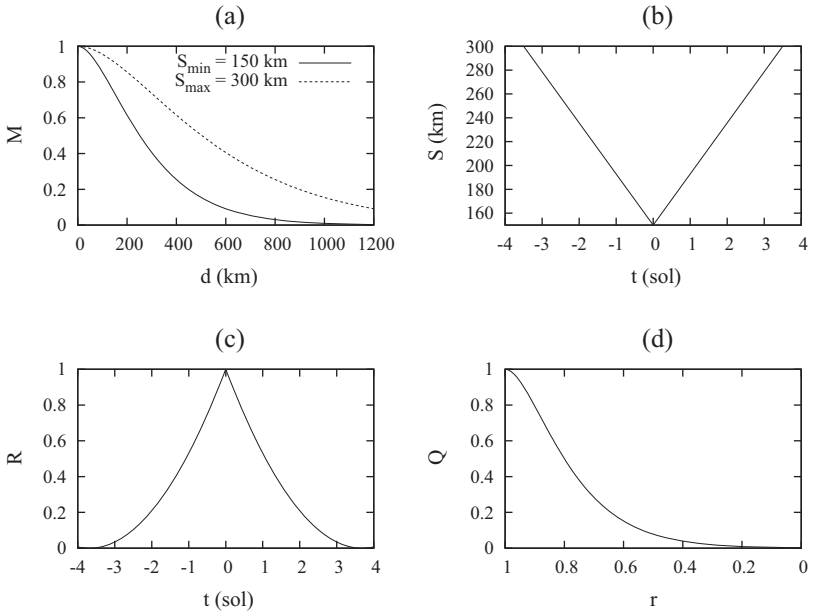

Fig. 4. Plots of the weighting functions used in Eq. (3). Panel (a) shows the distance weight M as a function of d (see Eq. (6)) for two different values of correlation scale S, corresponding to $S_{min} = 150$ km and $S_{max} = 300$ km. The S function (see Eq. (3)) is plotted in panel (b), as a function of t over the range $-3.5 < t < 3.5$ for TW = 7 sol. In panel (c) we plot the time weight function R (see Eq. (8)) for the same TW = 7 sol. The value of the R function at the extrema of the time window interval is fixed to 0.05 in this work. Finally, panel (d) shows the plot of the quality weight Q (see Eq. (9)) as a function of the reliability value r.

number of observations to grid, and (2) simple box averages introduce temporal and spatial biases if long time intervals and/or large spatial boxes are used (several orbits at different times are inevitably averaged together).

Reconstructing the dust climatology while preserving the short time and spatial variability of dust storms requires a more sophisticated data gridding. In order to achieve this objective, we have developed an efficient 'iterative weighted binning' methodology, described in the following Section.

3.1. The principle of iterative weighted binning (IWB)

The application of our gridding procedure is equivalent to a moving weighted average characterized by the use of successive spatio-temporal windows. The basic principle of the methodology is that, for a given grid point at a given time, all observations within a defined time window and spatial range are averaged using weights that depend on (1) the interval between the time of each observation and the time at the grid point, (2) the spatial distance between each observation location and the location of the grid point, and (3) the quality of each observation.

The weighted average value Y at a given time t_0 and location $\mathbf{x}_0$ for a generic observed variable y, which is a function of time and spatial coordinates, is given by:

$$Y(\mathbf{x}_0, t_0) = \frac{\sum_{n=1,N} M(\delta\mathbf{x}_n, \delta t_n) \cdot R(\delta t_n) \cdot Q(r_n) \cdot y_n(\mathbf{x}_n, t_n)}{\sum_{n=1,N} M(\delta\mathbf{x}_n, \delta t_n) \cdot R(\delta t_n) \cdot Q(r_n)}, \qquad (2)$$

where n represents the index of the N observations $y_1, y_2, \ldots y_N$ that are included in a three- or four-dimensional (if the vertical dimension is included) bin defined around the time t_0 and the location $\mathbf{x}_0$. R is the time weighting function, which determines the contribution of the nth observation according to the time difference $\delta t_n = t_n - t_0$ (positive for observations in the future, negative for observations in the past). M is the distance weighting function, which determines the contribution of the nth observation according to its distance $\delta\mathbf{x}_n = |\mathbf{x}_n - \mathbf{x}_0|$ from the location $\mathbf{x}_0$. The distance weight is also a function of the time interval δt_n so that observations at different times with respect to t_0 have different distance weights. This choice takes into account the possible advection of the variable y toward/-away from the location $\mathbf{x}_0$. Finally, Q is the observation quality weighting function, which determines the contribution of the nth observation according to its reliability value r_n.

The particular choice for the form of the weighting functions M, R, and Q depends on the specific application. For our purpose of gridding orbiting satellite observations, it is convenient to use weighting functions similar to those implemented in the analysis correction data assimilation scheme of the UK Meteorological Office (Lorenc et al., 1991) and in the derived Mars analysis correction data assimilation scheme (Lewis et al., 2007). In fact, Eq. (2) applied to k grid points of a regular grid can be considered as the weighted average equivalent of the model grid point increment Eq. (3.18) in the analysis correction scheme of Lorenc et al. (1991), although this analogy has no formal basis.

Eq. (2) applies to observations in a specifically defined time window and space range. Our methodology includes the iterative use of less and less restrictive time windows and space ranges, as we explain in the next section where we describe the application of the IWB to the problem of gridding dust optical depth observations.

3.2. Gridding with IWB: procedure

We have mentioned in Section 2.2 that our working variable is the IR column dust optical depth (in absorption at 9.3 μm) normalized to 610 Pa, which we henceforth indicate simply as τ. Note that, when Eq. (1) is used in Eq. (2), 610 Pa is factorable, hence the description of the procedure is in fact applicable to column optical depth values normalized by the surface pressure (with unit of Pa^{-1}), and any arbitrary reference pressure level can be used.

If we apply Eq. (2) to each grid point k of a pre-defined longitude-latitude-time grid for the variable τ, the weighted average value T at each grid point can be written as:

$$T_k = \frac{\sum_{n=1,N} M(d_{nk}, t_{nk}) \cdot R(t_{nk}) \cdot Q(r_n) \cdot \tau_n}{\sum_{n=1,N} M(d_{nk}, t_{nk}) \cdot R(t_{nk}) \cdot Q(r_n)}, \qquad (3)$$

where $\tau_1, \tau_2, \ldots \tau_N$ are the observations included in a specified time window and space box defined around the time and location of the grid point k, d_{nk} is the spatial distance from observation n to grid point k, t_{nk} is the time difference between observation time and grid point time, and r_n is the reliability value associated with the nth observation. In this work we use the Mars Universal Time (MUT) of the prime meridian as reference time. The beginning of a sol occurs at 00:00 MUT and the end at 24:00 MUT. The time of an observation, as well the time of all the grid points on a global longitude-latitude map, are expressed in term of martian year, sol, and its fraction. For each observation, we use the spacecraft clock, the longitude, and the local time to convert to the reference time. Time differences between observations and grid points, therefore, are calculated with respect to the prime meridian. We use the haversine formula to calculate the distance between two locations on the spherical planetary surface, which is numerically better conditioned for small distances (Sinnott, 1984).

We define the weighted root mean squared deviation (RMSD, equivalent to the biased weighted standard deviation) associated with the weighted average value T_k as:

$$s_{T_k} = \sqrt{\frac{\sum_{n=1,N} M_{nk} \cdot R_{nk} \cdot Q_n (\tau_n - T_k)^2}{\sum_{n=1,N} M_{nk} \cdot R_{nk} \cdot Q_n}} = \sqrt{\frac{\sum_{n=1,N} M_{nk} \cdot R_{nk} \cdot Q_n \cdot \tau_n^2}{\sum_{n=1,N} M_{nk} \cdot R_{nk} \cdot Q_n} - T_k^2}, \quad (4)$$

and the combined uncertainty of the weighted average as:

$$e_{T_k} = \sqrt{\frac{\sum_{n=1,N} (M_{nk} \cdot R_{nk} \cdot Q_n \cdot e_{\tau_n})^2}{\sum_{n=1,N} (M_{nk} \cdot R_{nk} \cdot Q_n)^2}}, \quad (5)$$

where e_{τ_n} is the uncertainty of the single optical depth observation. The former provides an estimate of the degree of homogeneity or variability of the gridded observations, the latter provides an estimate of the precision of the grid point average.

We choose M to be a second-order autoregressive correlation function of the distance d_{nk} and of the correlation scale S (see also Eq. (3.19) in Lorenc et al., 1991):

$$M_{nk} = (1 + d_{nk}/S(t_{nk})) \exp(-d_{nk}/S(t_{nk})), \quad (6)$$

where $S(t_{nk})$ is a function of the time difference. S is chosen to be a linearly increasing function of this difference, symmetric with respect to $t_{nk} = 0$, with a minimum value S_{min} at $t_{nk} = 0$ and a maximum value S_{max} at the extrema of the chosen time window (TW). The equation for S (defined over the range $-\mathrm{TW}/2 < t_{nk} < \mathrm{TW}/2$) is therefore provided by:

$$S_{nk} = \frac{S_{max} - S_{min}}{TW/2} |t_{nk}| + S_{min}. \quad (7)$$

With this choice of S, observations with times closer to the time of the requested grid point have weights M_{nk} that decrease faster with distance (see Fig. 4). In other words, larger weights are assigned to distant observations when they are also distant in time. The idea is to take into account the possible advection of dust toward/away from the grid point during the time window. Two further parameters, lon_{cutoff} and lat_{cutoff}, set the longitude and latitude limits of the space box within which observations can contribute to the average ($-lon_{cutoff} \leqslant lon_{nk} \leqslant +lon_{cutoff}$ and $-lat_{cutoff} \leqslant lat_{nk} \leqslant +lat_{cutoff}$). The choice of using two distinct spatial ranges allows to take into account the smaller separation of observations in latitude than in longitude, avoiding too much smoothing in latitude while considering enough observations in longitude.

R is chosen to be a decreasing quadratic function of the time difference t_{nk} (Lorenc et al., 1991), symmetric with respect to $t_{nk} = 0$. The equation for R (defined over the range $-\mathrm{TW}/2 < t_{nk} < \mathrm{TW}/2$) is therefore:

$$R_{nk} = \left(\frac{R_{min} - 1}{TW/2} |t_{nk}| + 1 \right)^2, \quad (8)$$

where R_{min} is the minimum value at the extrema of the chosen time window (see Fig. 4 for an example with TW = 7).

Finally, Q is chosen as a second-order autoregressive correlation function of the reliability value of an observation, namely:

$$Q_n = \left(1 + \frac{(1 - r_n)}{\lambda}\right) \exp\left(-\frac{(1 - r_n)}{\lambda}\right), \quad (9)$$

where λ is a scaling factor used to obtain the desired width at half maximum (WHM) for the Q function. We choose $\lambda = 0.119165$ to have WHM = 0.8 (i.e. $Q = 0.5$ when the reliability value of an observation is 0.8). See Fig. 4 for a plot of the Q function we use.

For MY 24 and 25 we have used only TES observations. For MY 26 and 27 we have used both TES and THEMIS observations until $L_s \sim 80^\circ$ in MY 27, then only THEMIS observations. For MY 28, we have used only THEMIS until $L_s \sim 112^\circ$, then both MCS and THEMIS, as well as in most of MY 29, 30, and 31, apart from $L_s \sim 327^\circ$, MY 29, to $L_s \sim 24^\circ$, MY 30, when only THEMIS observations are available.

We have tested the sensitivity of the method to different spatial and temporal resolutions and the results are reported in Section 3.3. On the basis of the sensitivity tests, we have chosen for TES in MY 24, 25, and TES + THEMIS in MY 26, a fairly high resolution (particularly in latitude), namely $6^\circ \times 3^\circ$ longitude $\times$ latitude. It is not advised to use the same resolution in latitude for MCS, given the fact that the path of the limb observations usually spans several degrees in latitude, and there are fewer observations per degree than TES. The sparse distribution of THEMIS observations must also be taken into account in the choice of the spatial resolution when only THEMIS data are available. In order to maintain a consistent resolution throughout MY 27, 28, 29, 30 and 31, we use $6^\circ \times 5^\circ$ longitude $\times$ latitude.

The choice of the time resolution is one sol. This means that the IWB procedure is applied to spatial grid points every sol, when the reference MUT time is 12:00 h (by convention). Because in our work most of TES observations have local times close to 14:00 h and most of MCS observations have local times close to 03:00 h, the observations that have shorter time difference with respect to the reference time of each map are located around 30°E in the TES years, and 135°W in the MCS years. The local time of the corresponding grid points, therefore, is closer to the real local time of the respective observations. Because the local times of TES and MCS observations are mostly fixed, each daily map of our gridded product should be considered as a global map of observations at mainly fixed local times (except for grid points in the polar regions). When MCS dayside observations are available and averaged together with nightside ones, a slight variation in local time can be appreciated across the global map, depending on the time weights.

The following is a summary of our gridding procedure with IWB. The choice of the parameter values required by Eq. (3) for version 2.0 of our gridded map product is detailed in Table 1.

- At each iteration, for each grid point, we define a time interval and spatial box within which we use observations to calculate the weighted average and its associated weighted root mean square deviation and combined uncertainty, applying Eqs. (3)–(5).
- The criterion to accept a value of weighted average at a particular grid point at a given iteration is that there must be at least a minimum number of observations N_{thr} within a distance d_{thr} from the grid point. If this is not the case, a missing value is assigned to the grid point at that iteration.

Table 1
Parameters for the gridding procedure. This table summarizes the parameters used in the gridding procedure with IWB (v2.0) for the four combinations of datasets and for the different iterations. We have used 4 iterations of the procedure, mainly changing the time window. The superscripts indicate that the same parameter has been used for more than one iteration ('1' indicates the first iteration, etc.). Other parameters not included in this table are kept fixed in this work, i.e. the time resolution of the maps is 1 sol, the value of the R function at the extrema of the TW is 0.05, the value λ in Eq. (9) is 0.119165.

	Spatial grid (lon-lat)	TW (sols)	lon_{cutoff} (degrees)	lat_{cutoff} (degrees)	S_{min} (10^2 km)	S_{max} (10^2 km)	d_{thr} (10^2 km)	N_{thr}
TES	$6^\circ \times 3^\circ$	1, 3, 5, 7	$6, 9^{2,3,4}$	$3, 4.5^{2,3,4}$	$1.5^{1,2,3,4}$	$1.5, 3^{2,3,4}$	$2, 3^{2,3,4}$	$3^{1,2,3,4}$
TES + THEMIS	$6^\circ \times 3^\circ$	1, 3, 5, 7	$6, 9^{2,3,4}$	$3, 4.5^{2,3,4}$	$1.5^{1,2,3,4}$	$1.5, 3^{2,3,4}$	$2, 3^{2,3,4}$	$1^{1,2}, 3^{3,4}$
THEMIS	$6^\circ \times 5^\circ$	1, 3, 5, 7	$15^{1,2,3,4}$	$12.5^{1,2,3,4}$	$1.5^{1,2,3,4}$	$1.5, 3^{2,3,4}$	$3^{1,2,3,4}$	$1^{1,2}, 2^{3,4}$
MCS + THEMIS	$6^\circ \times 5^\circ$	1, 3, 5, 7	$6, 9^{2,3,4}$	$5, 7.5^{2,3,4}$	$1.5^{1,2,3,4}$	$1.5, 3^{2,3,4}$	$2, 3^{2,3,4}$	$3^{1,2,3,4}$

- We repeat the previous steps iteratively, using different time windows, from the smallest to the largest, and calculating the weights accordingly. At each iteration, more valid grid points are added to the global longitude-latitude map, because more observations are considered and contribute to the averages. Grid points flagged as valid in previous iterations are not overwritten, so that each grid point is valid within the shortest possible time window.
- The final result of the successive application of the weighted binning equation consists in a global map of CDOD normalized to 610 Pa, with missing values in places where the gridding criterion mentioned above is not satisfied at any iteration.

The IWB procedure is applied independently for each grid point, at each sol. Nonetheless, each observation can be used in several grid point averages, although weighted differently. Grid point averages flagged as valid in iterations with TW > 1 sol are obtained using observations common with antecedent or subsequent maps. On each map, the grid point spacing is such that observations are weighted averaged within overlapping longitude-latitude boxes. Grid point averages, therefore, have some degree of dependence upon each other.

3.3. Gridding with IWB: examples

In order to illustrate the procedure of gridding when the observation coverage is good both in space and time (at least for most latitudes), we use an example from TES observations in the northern winter of MY 24, at a time when a "flushing" dust storm occurred. Flushing storms develop in the northern plains and rapidly move southward, crossing the equator and usually attaining the size of large regional storms in the southern hemisphere (see e.g. Wang et al., 2003; Wang, 2007).

Fig. 5 highlights one of the main reasons why the application of weighted binning in space and time is beneficial. In this figure, TES observations are shown within a time window of 7 sols (about 5° solar longitude at this season), centered around 12:00 MUT in sol-of-year 449, $L_s = 227.1^\circ$, MY 24 (see Appendix A for a description of the sol-based martian calendar we use in our work). The area shown in the figure is limited to 80° longitude and 40° latitude south of the equator. The colors indicate the time difference between the observations and the reference time. It is clear that adjacent orbits have quite different times. A simple box average would introduce biases when producing a global map of τ for this sol, mixing observations obtained sols apart, and resulting in improper smoothing.

The application of the IWB with increasing time window length is shown in Fig. 6. We separate each iteration (TW = 1, 3, 5, and 7 sols), respectively showing the orbits of the retrieved τ, and the uniformly gridded values. Clearly, gridded values of τ with larger TWs are smoothed with respect to smaller TWs, even if time weighting is applied in both cases. The result of the successive application of the weighted binning is then shown in panel (c), where the valid grid points in each iteration add to the valid values

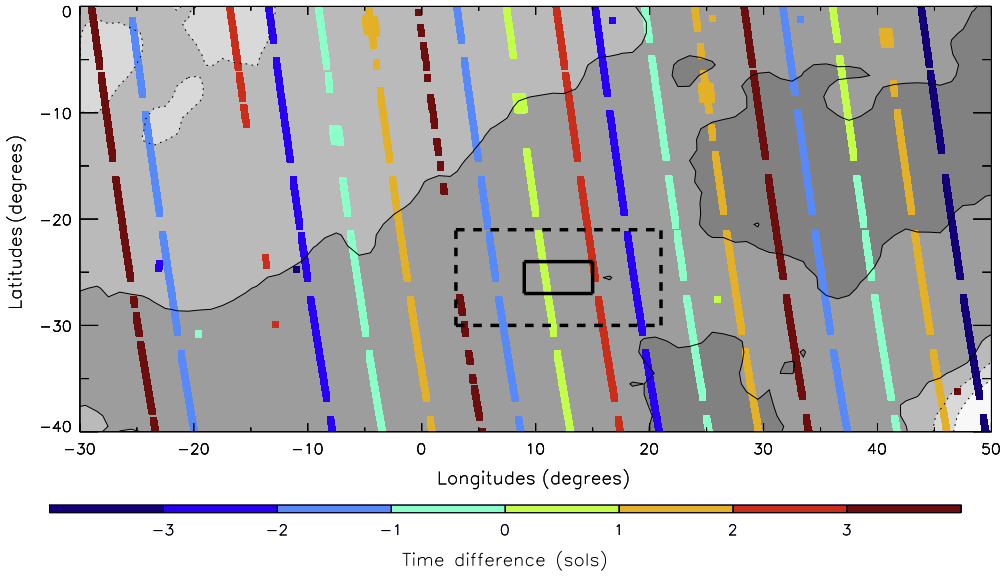

Fig. 5. The difference between the time of each TES observation and 12:00 h at 0° longitude (MUT) in sol-of-year 449, $L_s = 227.1^\circ$, MY 24. The observations are shown within a time window of 7 sols centered around 12:00 MUT. The picture is a zoomed view centered around 10° longitude and −25° latitude. The black solid square shows a $6^\circ \times 3^\circ$ longitude-latitude grid box whereas the black dashed square indicates the spatial box bounded by the lon_{cutoff} and lat_{cutoff} parameters we use in the weighted binning for the TES dataset when the time window is 7 sols (see Table 1). We apply the time and spatial weighting for observations within the dashed box, as detailed in Section 3.2.

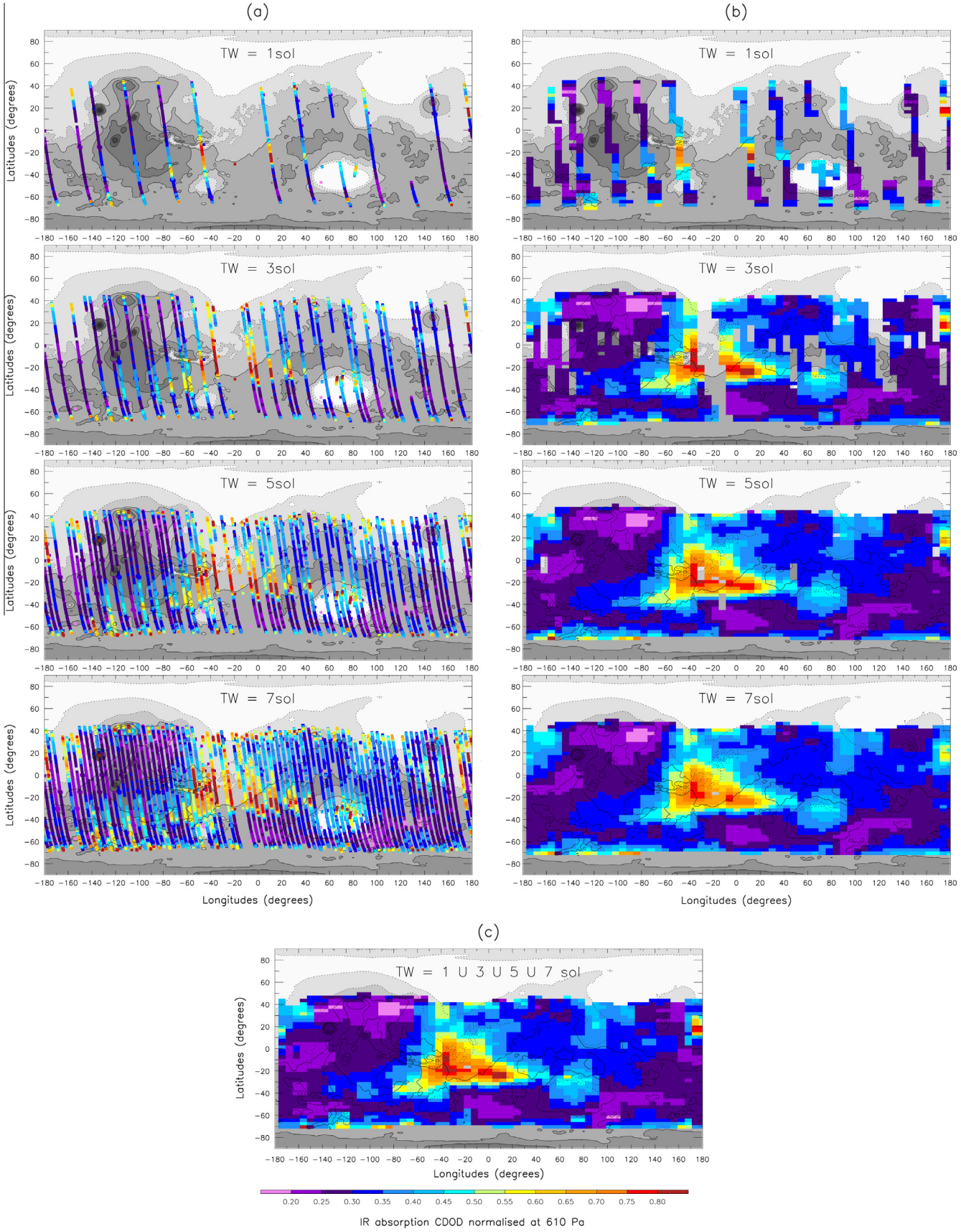

Fig. 6. (a) The panels from top to bottom show TES dust optical depth retrievals accumulated within time windows of 1, 3, 5 and 7 sol, centered around 12:00 MUT in sol-of-year 449, $L_s = 227.1^\circ$, MY 24. (b) The panels from top to bottom show the corresponding partial results of the application of the weighted binning for each specific time window. Finally, in panel (c) we show the result of the iterative application of all 4 TW, where the valid grid points in each previous iteration are not overwritten. There are 60×60 grid points in the gridded maps, separated by 6° in longitude and 3° in latitude. Missing values are assigned to bins where the acceptance criterion is not satisfied (see Table 1).

of the previous iterations, without overwriting. Eventually, we obtain a fairly complete, regularly-spaced map of τ, showing that an iterative weighted binning produces more valid and less biased values than the application of a single weighted binning with a fixed TW.

Ideally, the gridding method should not show much sensitivity with respect to the choice of reasonable spatial and temporal resolutions, particularly in the RMSD field. In order to verify the quality of the choice for the spatial resolutions, we have carried out a sensitivity test using four different cases, as illustrated in Fig. 7 for a typical map with large dust optical depth contrasts (same sol-of-year as in Fig. 6). Both averaged values and RMSD values – the latter representing the variability within the group of averaged observations – show little variation throughout the four cases. This result proves (at least for TES in good conditions of data

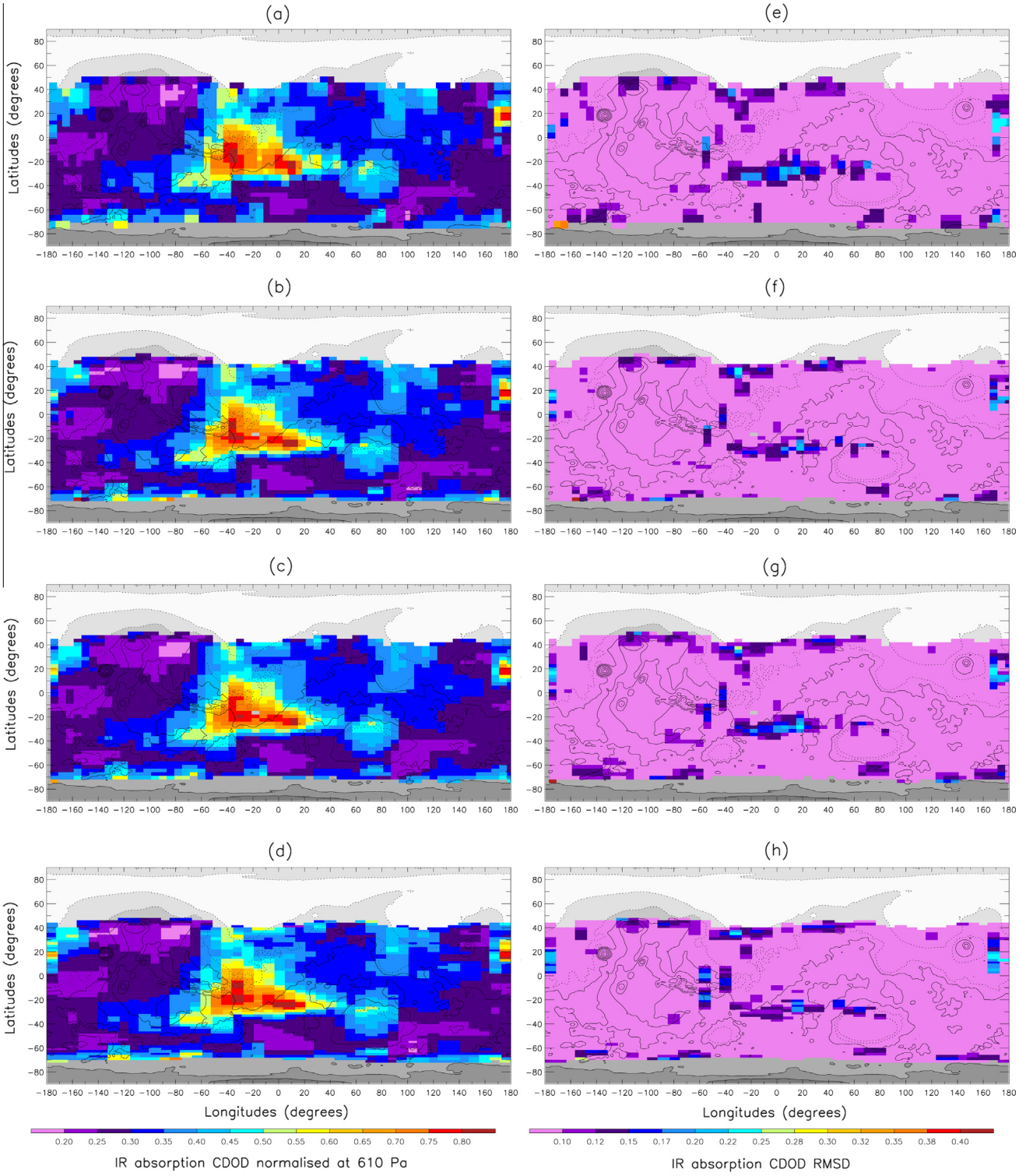

Fig. 7. Tests on the sensitivity of the gridding procedure to the spatial resolution. We use the same sol-of-year as in Fig. 6. Panel (a) and (f) show the case with $5^\circ \times 5^\circ$ longitude-latitude resolution, respectively in the average and in the root mean squared deviation (RMSD) fields; panel (b) and (g) are for the case with $6^\circ \times 3^\circ$ resolution; panel (c) and (h) are for the case with $6^\circ \times 3^\circ$ resolution but longer range for the space weighting ($S_{min} = 250$ km and $S_{max} = 400$ km); panel (d) and (i) are for the case with $8^\circ \times 2^\circ$ resolution.

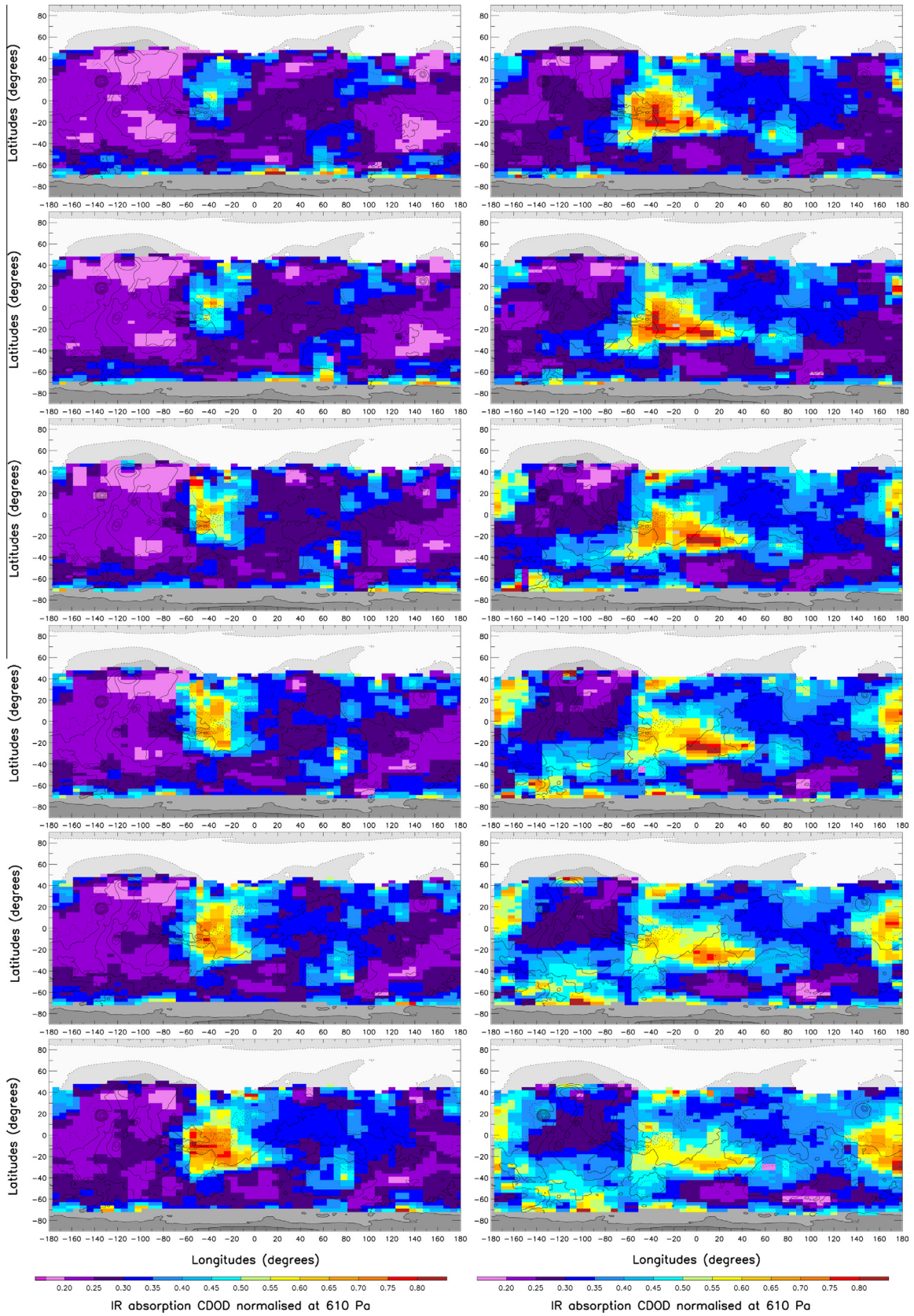

Fig. 8. Evolution of the MY 24, $L_s \sim 227^\circ$ flushing storm. Each panel shows gridded column dust optical depth (in absorption at 9.3 μm) normalized to the reference pressure level of 610 Pa. From top left to bottom right, maps are provided from sol-of-year 442 to sol-of-year 453 (i.e. from $L_s = 221.4^\circ$ to $L_s = 228.4^\circ$). In all panels, MUT is 12:00 h and solar longitudes are calculated for this time of the day. See also Appendix A for the description of the sol-based martian calendar we use in this paper.

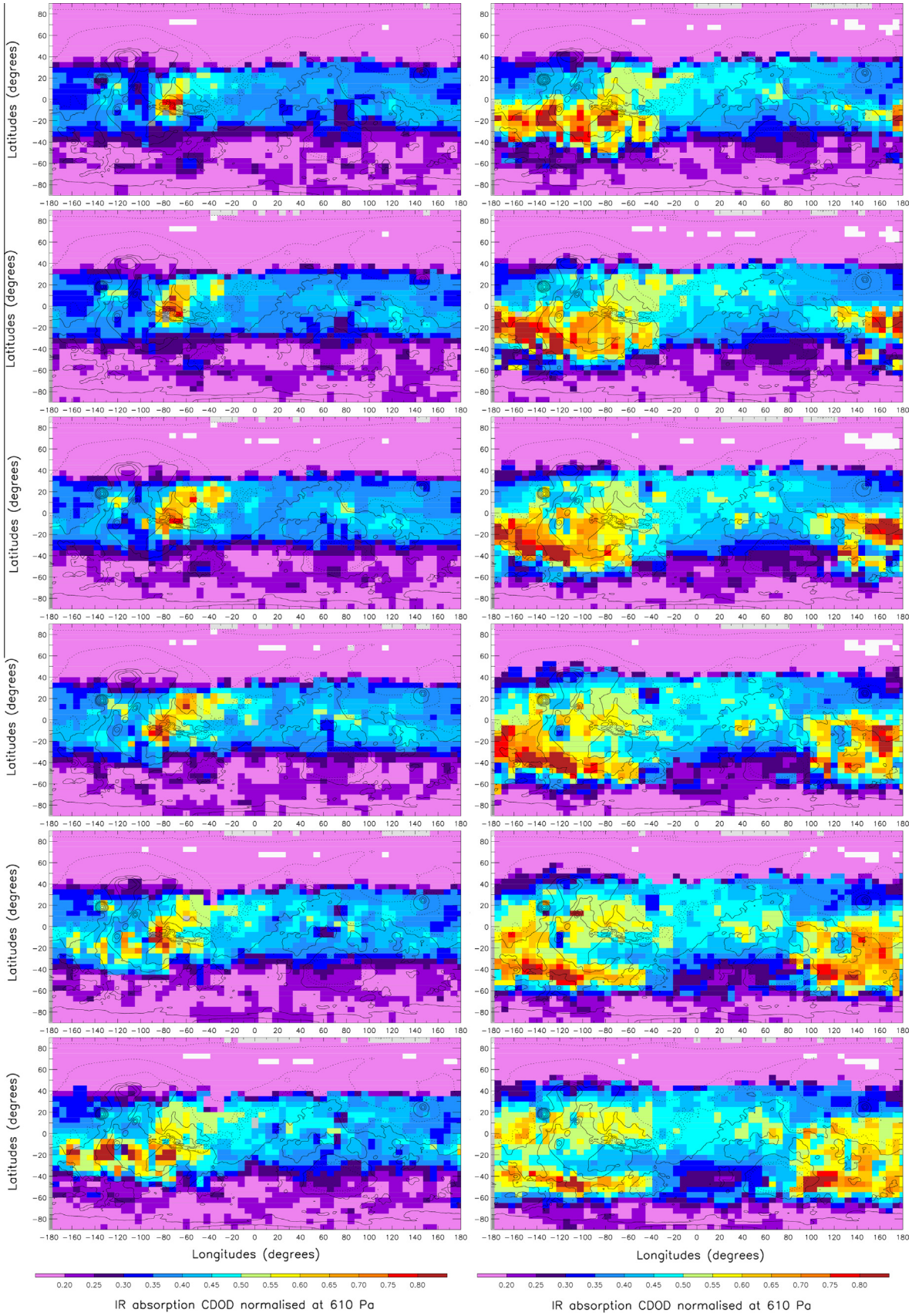

Fig. 9. Evolution of the MY 29, $L_s \sim 235^\circ$ regional storm. As in Fig. 8, each panel shows gridded column dust optical depth (in absorption at 9.3 μm) normalized to 610 Pa. From top left to bottom right, maps are provided from sol-of-year 457 to sol-of-year 468 (i.e. from $L_s = 232.3^\circ$ to $L_s = 239.4^\circ$).

coverage) that our gridding procedure is not particularly sensitive to the choice of the spatial resolution within a limited range.

The combination of Figs. 6, 8, and 9 provides the basis for our choice of the 1-sol time resolution. Ideally, we want the highest time resolution to follow the development of regional dust storms, using as many independent observations as possible. The top panels of the (a) and (b) series in Fig. 6 show that the main features of the regional storm occurring at $L_s = 227.1^\circ$ in MY 24 can be captured with a 1-sol TW gridding. Fig. 8 illustrates that, for the same period, we can precisely characterize the daily evolution of the storm, and Fig. 14 in Section 4.3 demonstrates that such daily evolution can be validated with MOC global visible images. TES has the advantage of a good spatial coverage and observation number even in condition of high aerosol loading, which is not always the case for MCS, particularly for dayside observations. Nonetheless, Fig. 9 shows that even during the MCS years we can nicely follow the daily evolution of regional storms (in this case we see a flushing storm occurring at $L_s \sim 235^\circ$ in MY 29). See also Section 4.3 for a discussion on the validation of the gridded maps with MARCI global visible images during this particular event.

It is worth stressing that the IWB procedure can theoretically be applied with a time resolution of a fraction of a sol, but because of the limitation in the number of satellite orbits per day, only certain longitudes can be updated and the degree of independance of the grid points decreases. If using full dayside and nightside orbits, though, a time resolution of half a sol would provide insights into the diurnal variability of τ (see also Section 7).

4. Validation of gridded maps

We have carried out a statistical validation of the τ maps based on two approaches:

1. an internal validation comparing TES, THEMIS, and MCS normalized optical depths to gridded values, interpolated in the locations of the observations;
2. an external validation using independent observations. These include the values of visible CDOD retrieved from CRISM observations, the time series of visible CDOD retrieved from PanCam cameras aboard Spirit and Opportunity and from the SSI camera aboard Phoenix, the time series of IR CDOD retrieved from Mini-TES aboard the two MERs, and some MOC and MARCI global images during the evolution of regional dust storms.

4.1. Internal validation

For the statistical internal validation, we have bilinearly interpolated the gridded maps at the location of each observation, if a complete set of neighbors was available (i.e. four adjacent spatial grid points). We have interpolated both the gridded average field and the combined uncertainty one, at the appropriate time (i.e. using the map of the sol corresponding to each observation).

The first test we have carried out is a simple correlation test. For all examined years, there is clearly a correlation between the observed values and the reconstructed ones, despite the application of the IWB method and the bilinear interpolation. High values of the Pearson correlation coefficient suggest a very good linear correlation in all years ($r \geqslant 0.93$ for TES in MY 24, 25, 26, $r = 0.96$ for THEMIS in MY 27, $r \geqslant 0.96$ for MCS in MY 28, 29, 30, 31), and the data points indeed accumulate around a straight line with slope close to 1 (not shown here).

We have then calculated the standardized mean difference (SMD) between an available interpolated value from the gridded maps (T_n) and an observed value (τ_n). This difference is weighted using the combination of the observation uncertainty (e_{τ_n}), and the interpolated combined uncertainty of the gridded average (e_{T_n}). Under the approximation that the observed value and the interpolated value are independent (i.e. the covariance is neglected), the variable we calculate for each observation n is:

$$\beta = \frac{T_n - \tau_n}{\sqrt{e_{T_n}^2 + e_{\tau_n}^2}}, \tag{10}$$

which is equivalent to expressing the difference between the two values in terms of their combined uncertainty. Strictly speaking, the interpolated value is not independent of the observed value because the latter has been used to calculate the former, so the value of β might be underestimated. Nonetheless, this variable is useful for estimating whether clear biases are present in our gridded maps, or whether the differences are within statistical limits.

We display in Fig. 10 the histograms of the SMD values for the TES (MY 24, 25, 26), THEMIS (MY 27), and MCS datasets (MY 28, 29, 30, 31). The difference in the number of values from year to year reflects the number of available retrievals, as shown in Figs. 2 and 3. All histograms show that most of the values have $|\beta| \leq 1$ (the difference is much lower than the combined uncertainty), with less than 1% of values each year having $|\beta| > 2$. Peak values are very close to zero ($\bar{\beta} < 0.08$ and positive), and standard deviations are reasonably small ($0.38 < \sigma_\beta < 0.55$). These general characteristics provide a sound internal validation from the statistical point of view. Other important factors to be considered are the shape of the histograms (i.e. skewness and kurtosis), which could highlight possible biases. All histograms are very symmetric (small skewness, particularly if we limit the values to $|\beta| \leq 2$), therefore no particular bias is evident. All distributions are leptokurtic (i.e. more sharply peaked than a Gaussian distribution), which indicates differences with respect to the combined uncertainty generally smaller than that expected by a random process. We have also specifically analyzed the SMD values for the two cases shown in Figs. 8 and 9, during the evolution of two regional dust storms. For the case of the MY 24 storm (sol-of-year 442–453), more than 95% of values are $|\beta| \leq 1$, the average is $\bar{\beta} = 0.01$ and the standard deviation is $\sigma_\beta = 0.46$. For the case of the MY 29 storm (sol-of-the-year 457–468), more than 98% of values are $|\beta| \leq 1$, the average is $\bar{\beta} = 0.03$ and the standard deviation is $\sigma_\beta = 0.32$. The SMD statistics for the specific cases of the regional dust storms, therefore, provides results in agreement with the general statistics.

A third diagnostic we use to internally validate our gridded maps is the relative RMSD of the grid points. This is expressed by the ratio between the weighted RMSD, calculated with Eq. (4) (a measure of the variability of τ at a grid point), and the weighted average calculated with Eq. (3). Fig. 11 shows that MY 24 and 26 have distributions peaked at values of relative RMSD lower than 10%, MY 25, 28, 29, 30, 31 have peaks around 10%, and only MY 27 has a peak around 20%. All years have very right-skewed distributions (particularly MY 26, which shows a long and almost linearly-decreasing tail), but the values of relative RMSD do not statistically exceed the values of the relative combined uncertainties. The yearly distributions of the latter have peaks around 20% (not shown here). Fig. 11, therefore, suggests reasonable values for the relative RMSD of the gridded maps, and provides an indirect validation of the goodness of the chosen spatio-temporal resolution. If the resolution was too coarse, in fact, one would expect large variability at most grid points, which is not the case here.

4.2. Validation with independent observations

We use independent CRISM retrievals of visible CDOD (900 nm wavelength) in MY 28, 29, and 30 to compare with gridded values interpolated in the position of CRISM observations, at the appropriate sol. As explained in Section 2.2, we have firstly divided

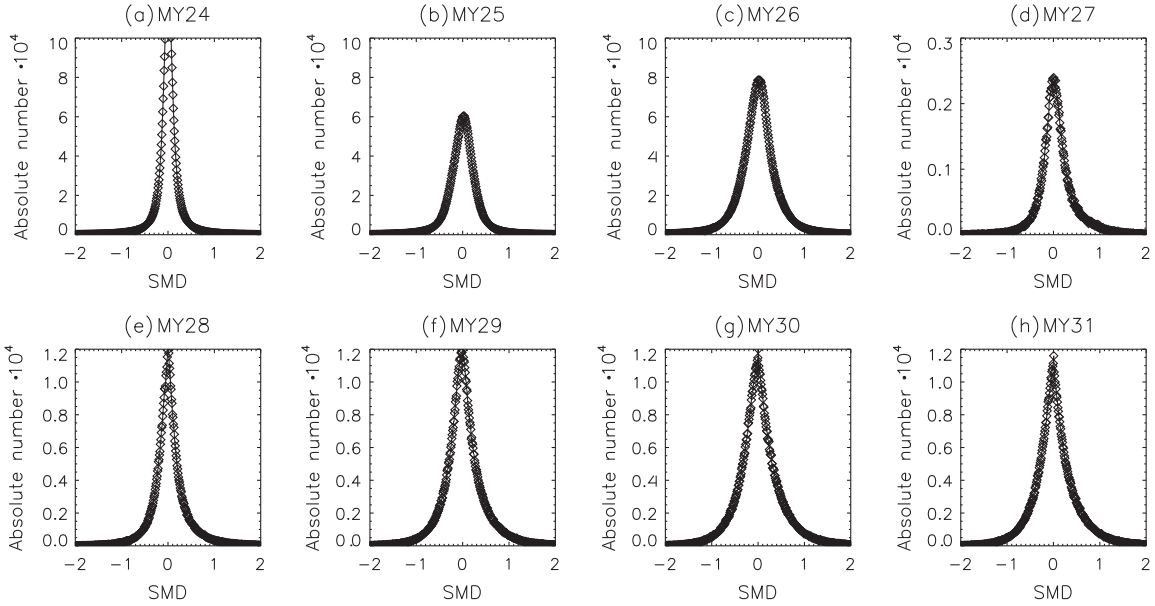

Fig. 10. Histograms of SMD values (Eq. (10)) for TES, THEMIS, and MCS datasets in different martian years: (a) TES, MY 24; (b) TES, MY 25; (c) TES, MY 26; (d) THEMIS, MY 27; (e) MCS, MY 28; (f) MCS, MY 29; (g) MCS, MY 30; (h) MCS, MY 31.

CRISM CDOD (normalized to 610 Pa) by a factor 2.6 to estimate equivalent IR absorption CDODs.

As in Section 4.1, we have calculated the Pearson correlation coefficients ($r = 0.78$ in MY 28, $r = 0.52$ in MY 29, and $r = 0.47$ in MY 30), and produced histograms of the SMD (Fig. 12) for each available year. The comparison with CRISM data produces much less correlated values and much more biased histograms than the internal validation. In particular, the SMD distributions are peaked around -1 and clearly left-skewed, which suggests a majority of largely underestimated τ values in the gridded maps with respect to those observed by CRISM. Systematic errors in the absorption-to-extinction, IR-to-visible, and 21.6 μm to 9.3 μm conversion factors, or their combination, can affect the average value of the SMD distributions. When dividing CRISM observations by conversion values larger than 2.6 (up to 3.5), the distributions tend to peak around zero, but the skewness is not significantly reduced (not shown here). From the validation with CRISM, therefore, the gridded maps in MY 28, 29, and 30 seem to underestimate the optical depth, and since no significant bias has been detected in the internal validation with MCS, one possible conclusion is that the MCS column optical depths are underestimated. Because no significant pattern in latitude or solar longitude can be detected in the distribution of the SMD values (not shown here), it is not possible to associate MCS extrapolations in particular conditions (e.g. high or low dust loading, presence of water ice, etc.) with the bias. CRISM CDODs, on the other hand, could be overestimated. At the time of writing, no satisfactory explanation could be found to address the MCS-CRISM bias, which could well originate from a combination of MCS underestimation, CRISM overestimation, and systematic errors in the conversion factors. This bias, therefore, requires further independent analysis to be fully understood.

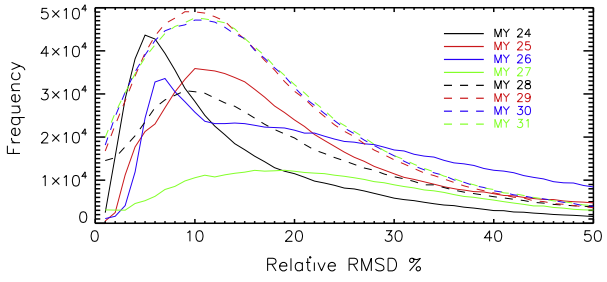

Fig. 11. Plot of relative root mean squared difference (RMSD) curves for all martian years. The relative RMSD is calculated as the ratio between Eqs. (4) and (3), for each valid grid point, and expressed as a percentage.

We also compare the gridded values, interpolated in the locations of the MER Spirit and Opportunity, to the CDOD measured by PanCam in the near-IR and by Mini-TES in the IR. The compared values, for each sol when there are available observations, are shown as time series in Fig. 13. This figure includes also the comparison to the CDOD measured by SSI aboard Phoenix in the near-IR. We have chosen to also display those years when MER and Phoenix observations are not available, in order to improve the statistics on interannual variability at Meridiani Planum, Gusev crater, and 'Green Valley' landing sites (see coordinates of locations in the caption of Fig. 13). As we have done for the comparison with CRISM, we have divided the PanCam and SSI near-IR observations by a factor of 2.6 to convert them to equivalent absorption IR, but we also show time series obtained using a minimum factor 1.5 and a maximum factor 3.0. All CDODs are normalized to 610 Pa.

The comparison in Gusev crater is satisfactory throughout the years and the seasons, with Mini-TES, PanCam and the gridded maps generally agreeing within the uncertainties (represented by the gray envelope), except for some Mini-TES peaks not seen as large by PanCam. Even in the clear seasons, the time series show consistency in all years, with values of τ between 0.10 and 0.15 on average, except for some apparent gaps in MY 29 and 30, which are still within the uncertainty envelope. These effects are described in Lemmon et al. (2015) as systematic, and at least in MY 29 they are possibly associated with the lack of calibration data.

The comparison in Meridiani is quite satisfactory during the dusty seasons but is problematic during the clear ones, when it highlights a strong difference between τ measured from the surface and from satellite observations. Consistently in every year, the gridded maps provide values that are about half of those observed by PanCam and Mini-TES during the period $L_s = [0°, 180°]$, well beyond the uncertainty envelope. This bias seems to be present in all three satellite datasets considered in this work, even when looking at single CDOD retrievals. Although the PanCam time series could lay at the upper limit of the uncertainty envelope if a maximum factor 3.0 is used, Mini-TES and the gridded maps (both providing values in the IR) are quite far apart.

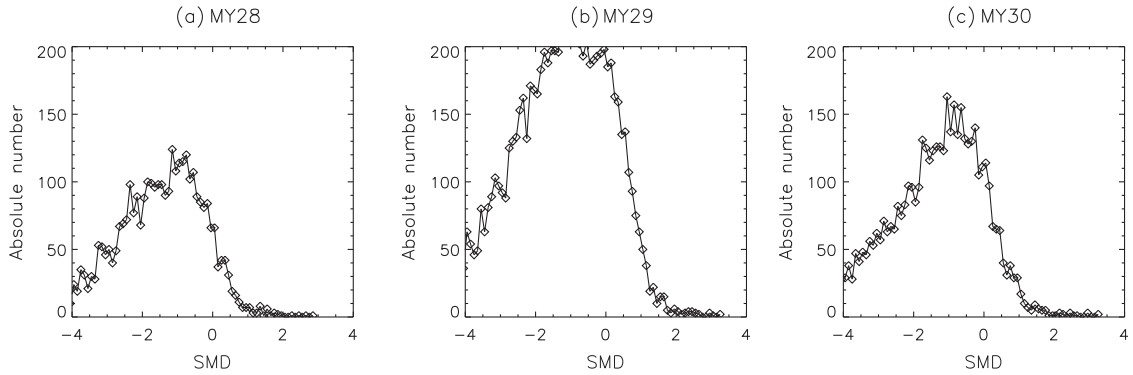

Fig. 12. Histograms of SMD values (Eq. (10)) for the CRISM dataset in different martian years: (a) MY 28; (b) MY 29; (c) MY 30.

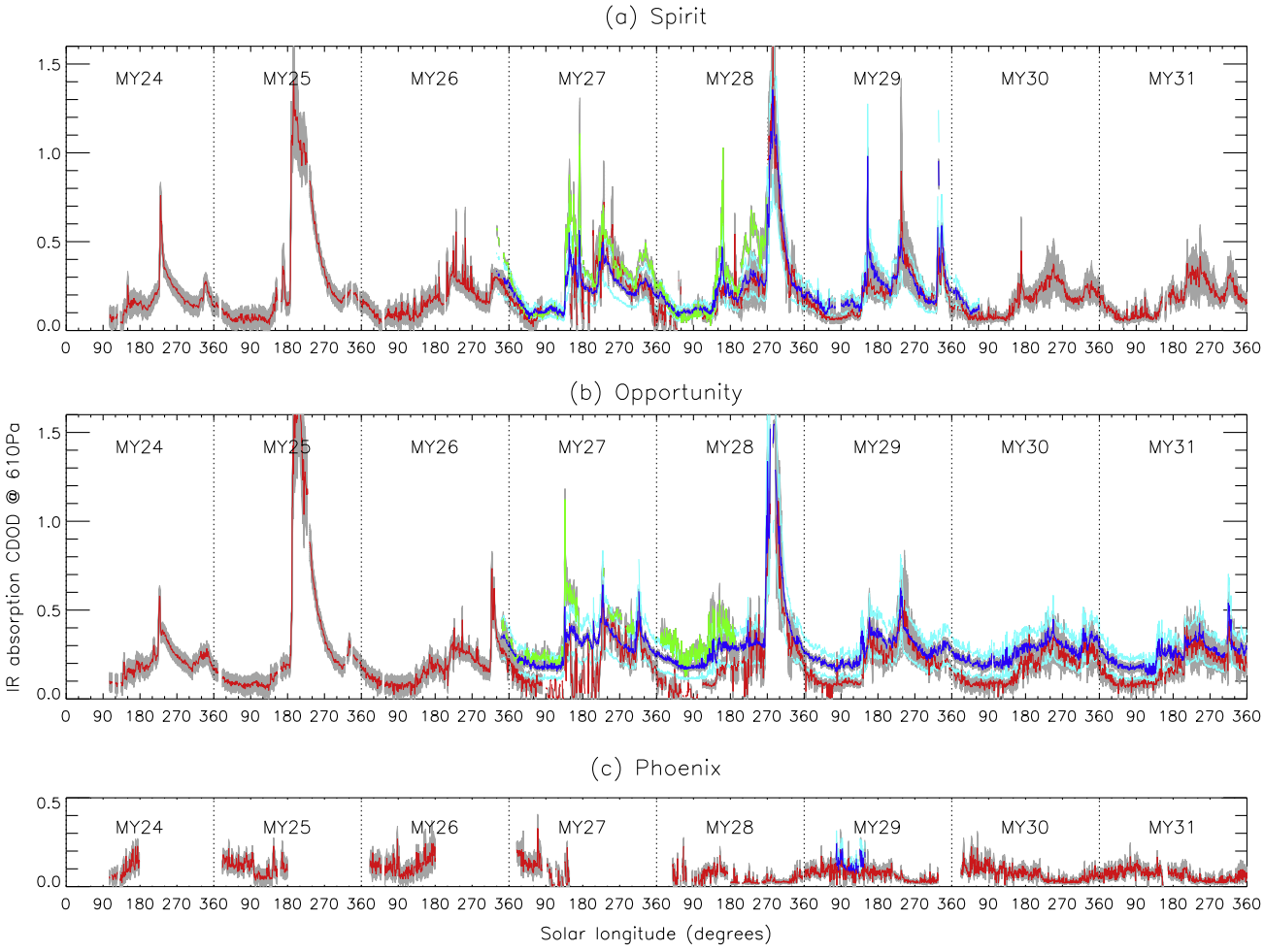

Fig. 13. Plot of column dust optical depth time series at (a) Spirit site in Gusev crater (175.48°E, 14.57°S), (b) Opportunity site in Meridiani Planum (354.47°E, 1.95°S), and (c) Phoenix site in 'Green Valley' (Vastitatis Borealis, 234.25°E, 68.22°N). The red curves are the time series of bilinearly interpolated values from the daily gridded maps obtained with the IWB procedure (if the 4 neighbor grid points are not all valid, the average of at least 2 valid neighbors is used instead of the bilinear interpolation). The green curves are sol-averaged values from MER Mini-TES, and the blue curves are sol-averaged values from MER PanCam in panels (a) and (b), and Phoenix SSI in panel (c). Corresponding uncertainties are drawn as overlapping gray envelopes. For the gridded maps, we choose the maximum value between the RMSD and the combined uncertainty at the interpolated location. For the other instruments, we follow what described in Section 2.3.3. Values from PanCam and SSI are divided by 2.6 to convert them into equivalent absorption IR, and compare to interpolated values from the gridded maps and Mini-TES values at 9.3 μm. The cyan curves represent PanCam and SSI time series when minimum and maximum factors of 1.5 and 3.0 are used instead of 2.6 (see also Section 2.3.4). All values of optical depth are normalized to 610 Pa. (For interpretation of the references to color in this figure legend, the reader is referred to the web version of this article.)

Lemmon et al. (2015) have recently provided a possible explanation for this bias in PanCam observations. According to them, water ice clouds and hazes contributed to the observed opacity at the Opportunity site in the summer season. Clouds were seen over the range $L_s = [20^\circ, 136^\circ]$, with peak activity near $L_s = 50^\circ$ and $L_s = 115^\circ$, whereas ice clouds and hazes were not seen at the Spirit site. When looking at the Sun through the atmospheric column, PanCam in Meridiani is likely to add water ice optical depth to the dust optical depth, thus possibly explaining at least part of the bias. TES shows that the time of discrepancy is also the time

when water ice peaks in Meridiani, with IR optical depths in the range 0.1–0.15 during much of aphelion (Smith et al., 2003). Although water ice could be a reasonable explanation for the high opacity values measured by PanCam at Meridiani, the same explanation cannot be applied straightforwardly to Mini-TES, which in principle should be able to distinguish between dust and water ice. Nevertheless, it should be considered that Mini-TES measurements of water ice are particularly difficult, as clouds are likely to be located above the dust layer, and the thermal contrast between the atmosphere and the sky is not as good as the contrast between atmosphere and surface for satellite instruments. It is worth noting that the gap between PanCam values and gridded values reduces rapidly in a short time interval after $L_s = 130^\circ$. This applies to the Mini-TES/PanCam ratio as well. Whether it is an effect of change in size or composition of aerosols, water ice diminishes quickly, but does not disappear at that L_s. Although the gap is larger around summer solstice, the gap between PanCam (as well as Mini-TES) and the gridded values is still important at times where no ice has been reported, for instance at $L_s \sim 0^\circ$ or $L_s \sim 180^\circ$. Water ice, therefore, cannot be the only reason why satellite instruments measure less dust optical depth than ground instruments at Meridiani. Further analysis needs to be done and/or independent observations need to be acquired to fully understand this important discrepancy.

Despite the bias in the absolute value of τ, it is very important to highlight the fact that the time correlation and the shape consistency of the different time series is striking, even during the MY 28 planet-encircling dust storm, when far fewer MCS observations are available for the gridding. The only exception is MY 27 and the beginning of MY 28, when only sparsely distributed THEMIS observations are available and the signal is much more noisy. When comparing the time series in Gusev and Meridiani over the eight available years, we can clearly observe and confirm from previous studies (e.g. Vincendon et al., 2009) that (1) the two planet-encircling dust storms (MY 25 and 28) had similar rapid growth, comparable peak values, and slow decay; (2) there are many regional storms that affected both Meridiani and Gusev (on the opposite side of Mars), reaching comparable peak values; (3) there is a tendency – with some exceptions – to have three distinct peaks of τ every second half of the year; an early, less pronounced peak around $L_s = 160^\circ$ (but in MY 27 it was as early as $L_s \sim 135^\circ$), a major peak around $L_s = 240^\circ$ (with the exception of MY 25, which was characterized by an equinoctial planet-encircling storm lasting well beyond $L_s = 240^\circ$), and a late peak around $L_s = 330^\circ$. The presence of three seasonal peaks of dust optical depth is not only confined to the equatorial latitude band, as discussed in Section 5 and shown in Fig. 16. Overall, the comparison with PanCam and Mini-TES time series confirms that the gridded maps are able to represent rapidly-evolving dust events with elevated optical depth. Both the timing and duration of the equatorial events are consistent with ground-based observations.

This conclusion extends to the northern high-latitude region, where the gridded values and SSI aboard Phoenix show consistent values of τ, although the availability of data from SSI is very limited. It is worth noting that the values observed by MCS and those observed by TES in the range $L_s = [90^\circ, 180^\circ]$ have mostly opposing tendencies. MCS observes decreasing values of opacity (consistent with SSI observations), except in MY 28, while TES measures increasing values. Further analysis would be required in this case as well to establish whether a systematic bias is present between the two datasets at these high latitudes in summer.

4.3. Validation of dust storm evolution using camera images

We have used MOC and MARCI daily global images (Cantor et al., 2001) to qualitatively compare the evolution of the two selected regional storms shown in Section 3.3. Fig. 14 shows the evolution of the flushing storm occurring in MY 24 at $L_s \sim 227^\circ$ (the separation between two consecutive panels is two sols), and Fig. 15 shows two sols during the evolution of the storm occurring in MY 29 at $L_s \sim 235^\circ$.

Although the color contrast between the dust and the background in both MOC and MARCI images makes it difficult to clearly visualize the presence of dust, the satellite observations help to characterize the spatial extent of the evolving storms. In MY 24, the contours of gridded τ correlate remarkably well with the presence of the dust haze in the MOC images, as well as with the individual TES retrievals along MGS orbits. This validation of the gridded maps during a particularly dynamic and rapidly evolving event encourages their use for statistical analysis of the evolution of dust storms, particularly in MY 24, 25 and 26 when a large number of TES retrievals are available.

In panels (a) and (c) of Fig. 15 we show the estimated values of τ along the nightside orbits of MCS, together with contours showing the spatial variation of the gridded values. Only nighttime profiles are adequate for yielding acceptable estimates of column optical depth in this case, after the application of the quality control procedure described in Section 2.1.2. In panels (b) and (d) the MARCI images are overlaid with the tracks of dayside (15:00 h) surface temperature anomaly, which serves as an alternative estimate of the presence and amount of dust. The observed surface temperature is actually top-of-atmosphere brightness temperature at 32 μm, where the atmosphere is relatively transparent. We plot the reduction in brightness temperature that largely reflects the cooling of the surface due to the depletion of daytime solar radiation by aerosol (relative to clear sky conditions). Wilson et al. (2011) devised a technique to estimate the CDOD from satellite observations of surface temperature. The technique uses a GCM with dust transport capability (the GFDL MGCM) to find the value of dust optical depth at any given time and location that yields the best match between observed and simulated brightness temperatures. They applied this technique to estimate CDODs during the MY 25 planet-encircling dust storm using TES observations, and in principle the same technique can be applied to MCS observations of brightness temperature. Given the fact that brightness temperature observations are available even when proper CDOD retrievals fail (particularly during dayside conditions), the gridding procedure would certainly benefit from the inclusions of CDOD data estimated as described above.

In the case of the MY 29 storm, the correspondence between the gridded τ values and the visual imagery is not as good as in the case of the MY 24 storm. In particular, the MCS (nighttime) retrievals appear to miss the presence of dust at the higher southern latitudes, especially during the early stages of the storm event (panel b). This issue will be discussed in more details in the next Section 5. Furthermore, nightside optical depths and dayside surface temperature anomalies (as well as dust hazes in the MARCI images) do not seem to correlate in latitude, although the correlation between single optical depth estimates and gridded values is satisfactory. The location of the storm in both sols appears more equatorward in the nightside observations than in the dayside ones. We cannot rule out the fact that the storm changed location between day and night, which points to the necessity of using as many MCS dayside retrievals as possible in future developments of our methodology, as compatible with the constraints described in Section 2.1.2.

5. Multiannual dust climatology

The daily maps of dust optical depth spanning eight martian years allow for the analysis of interseasonal and interannual variabilities. We have shown that one can follow the evolution of

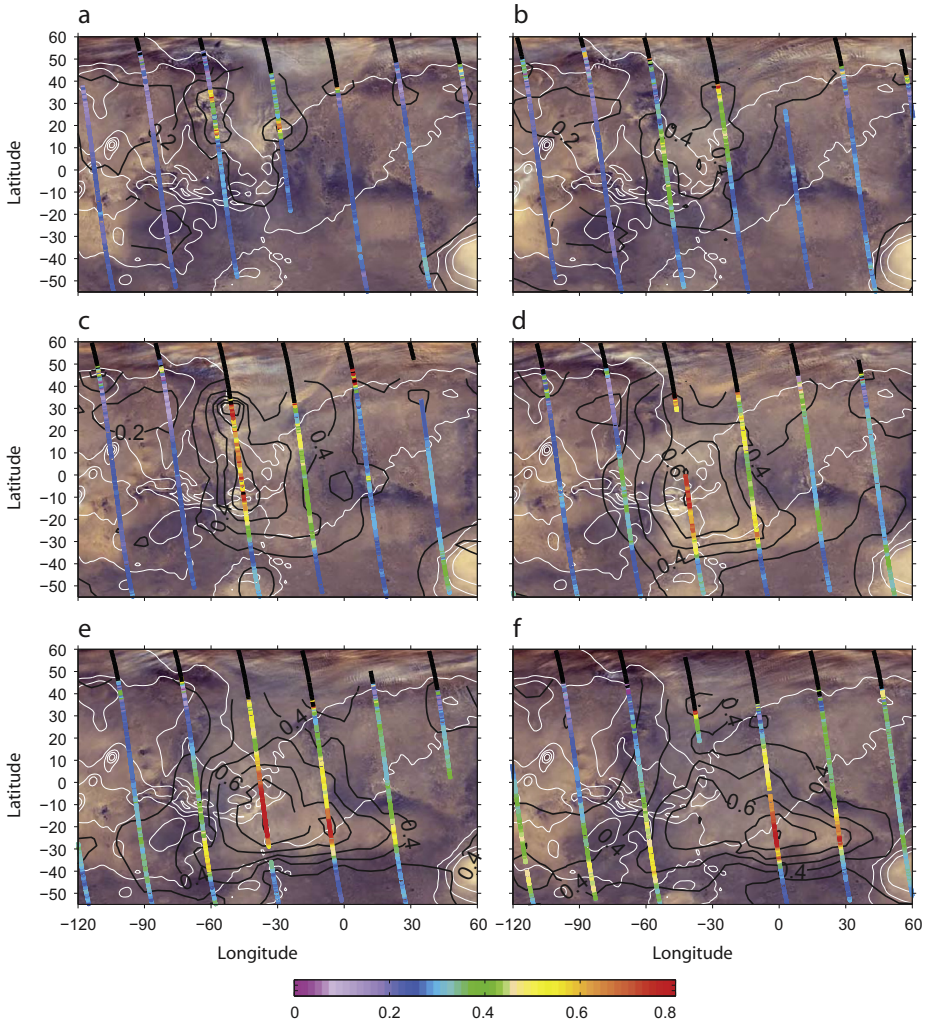

Fig. 14. TES orbits, color-coded using the normalized column dust optical depth (at 9.3 μm in absorption) and overlaid on MOC daily global images for 6 sols at 2 sol intervals in MY 24. Black squares show available TES observations but unavailable dust optical depth retrievals. Black contours show the optical depth derived from the gridded maps as described in the text. White contours show the local martian topography. (a) Sol-of-year 440, $L_s = 221.4^\circ$ (October 09, 1999), (b) sol-of-year 442, $L_s = 222.6^\circ$ (October 11, 1999), (c) sol-of-year 444, $L_s = 223.9^\circ$ (October 13, 1999), (d) sol-of-year 446, $L_s = 225.2^\circ$ (October 15, 1999), (e) sol-of-year 448, $L_s = 226.5^\circ$ (October 17, 1999), and (f) sol-of-year 450, $L_s = 227.8^\circ$ (October 19, 1999). The provided solar longitude values are those at 12:00 MUT of each sol. See Appendix A for the description of the sol-based martian calendar we use in this paper. MOC images are simple cylindrical projection at a resolution of 6 km/pixel (10 pixels/degree), recorded between 00:00 and 24:00 UTC of the indicated Earth day. (For interpretation of the references to color in this figure legend, the reader is referred to the web version of this article.)

individual regional dust storms when the gridded maps are fairly complete. Even when the number of valid grid points in the daily maps is low, the dust variability can still be analysed statistically, provided data are averaged or filtered to prevent contamination from spurious values (“outliers”) occurring at high frequencies (e.g. “on/off”, isolated, large optical depths).

We provide an animation of daily, irregularly gridded maps for each available martian year as supplementary material to this paper. The reader can therefore explore the entire time series that forms the current version 2.0 of the dust climatology obtained with IWB, before downloading the corresponding NetCDF dataset from the LMD website (at the address reported in the footnote of Section 1). The animation is organized as 669 frames (one for each sol-of-year) with eight maps on each frame corresponding to the available martian years. See also Appendix A for a description of the sol-based martian calendar we use in the present work.

The structure of the animation helps the analysis of the interannual variability. It is interesting, for instance, to look simultaneously at the dust optical depth around sol-of-year 360 ($L_s \sim 173^\circ$) in MY 24, 25, and 26, a few sols before the onset of the MY 25 planet-encircling dust storm. It appears clearly that the dust distribution was very similar in the three years observed by TES at this season, until sol-of-year 372 ($L_s \sim 180^\circ$), when slightly higher dust optical depth values appeared in the Hellas basin in MY 25, prior to the expansion towards the northern rim of the crater and out in Hesperia Planum.

The latitudinal, seasonal, and interannual variability of CDOD can be fully appreciated in Fig. 16, which summarizes eight years of dust climatology on Mars. We also provide the same type of figure with separated instrumental contributions (i.e. only TES, only MCS, and only THEMIS) as supplementary material to this paper, for reference and instrumental bias check. These figures highlight four distinctive phases in the distribution of dust during the second half of each year without a global-scale storm, and confirm (using the longest available record of observations) what other studies have found (e.g. Wang and Richardson, 2015; Kass et al., 2014). Aerosol dust starts to increase around $L_s = 150^\circ$ at equatorial/tropical latitudes in the southern hemisphere, including some enhanced southern polar cap edge increase after $L_s = 160^\circ$. The largest increase by far usually occurs between $L_s = 210^\circ$ and 240°, when baroclinic activity at high northern latitudes favors cross-equatorial flushing storms (although not all regional storms

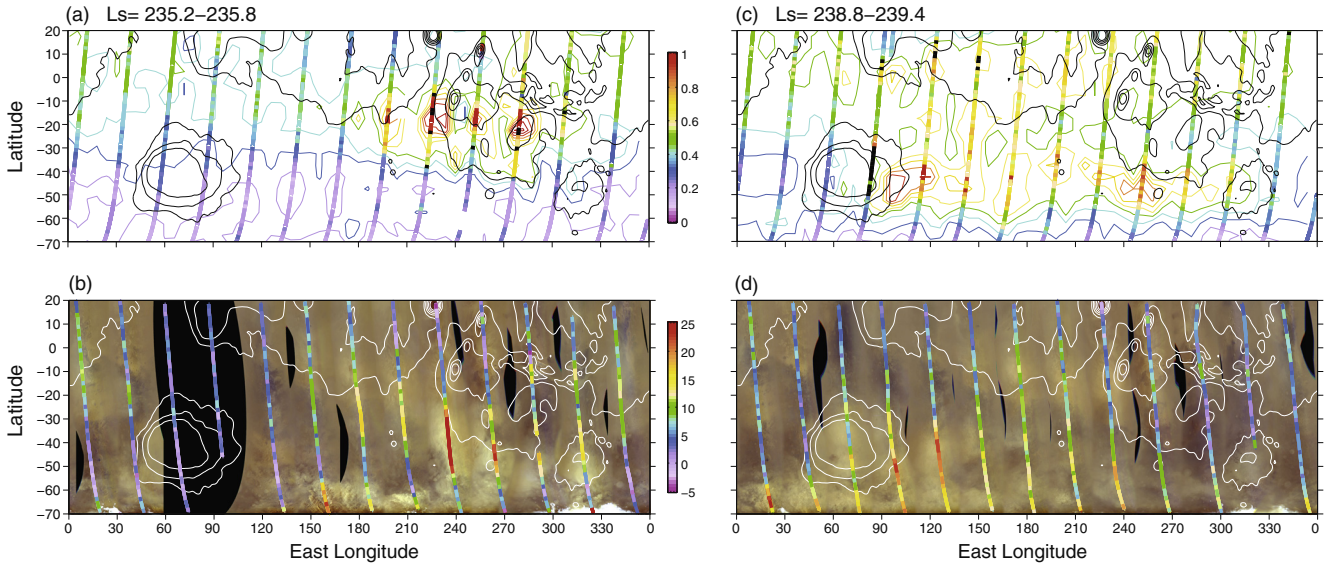

Fig. 15. The upper panels of this Figure show 2 sols of MCS nightside orbits in MY 29, color-coded using the normalized column dust optical depth (at 9.3 μm in absorption) and overlaid on color-coded contours of optical depth derived from the gridded maps. Black squares show available MCS observations but unavailable dust optical depth retrievals. Black contours mark the martian topography. The lower panels show the corresponding MCS dayside orbits, color-coded using the brightness temperature anomaly, and overlaid on MARCI daily global images. White contours mark the martian topography in this case. (a) and (b) Sol-of-year 462, $L_s = 235.5^\circ$ (March 28, 2009). (c) and (d) Sol-of-year 468, $L_s = 239.4^\circ$ (April 2, 2009). The provided solar longitude values are those at 12:00 MUT of each sol. See Appendix A for the description of the sol-based martian calendar we use in this paper. Brightness temperature anomaly is the apparent decrease in afternoon surface temperature (32 μm brightness temperature), relative to a clear atmosphere, that can be attributed to the influence of dust. MARCI images have a resolution of 6 km/pixel (10 pixels/degree), and are recorded in the solar longitude ranges (b) $L_s = [235.2^\circ, 235.8^\circ]$ and (d) $L_s = [238.8^\circ, 239.4^\circ]$. (For interpretation of the references to color in this figure legend, the reader is referred to the web version of this article.)

occurring at this time originate in the northern plains). A third phase in the dust distribution is characterized by large lifting of dust occurring in the southern polar region between $L_s = 250^\circ$ and 300°, after the CO_2 ice has mostly sublimated away. At other latitudes, in contrast, there is a clear decrease of atmospheric dust in every martian year after $L_s \sim 260^\circ$ (with the exception of MY 28, characterized by the late planet-encircling storm). This pause in large dust storms coincides with the decrease in the amplitude of low-altitude northern baroclinic waves (the so-called "solsticial pause", see e.g. Basu et al., 2006; Kahre et al., 2011; Read et al., 2011; Wilson, 2011; Mulholland, 2012). When the solsticial pause is over, and the baroclinic wave activity at low altitude reinforces again, the probability of late flushing storms increases. Every year, therefore, a fourth phase in the dust distribution starts around or after $L_s \sim 310^\circ$, producing a late peak of dust optical depth.

The fairly repeatable pattern of background or average dust optical depth from year to year contrasts with the highly unpredictable occurrence of global-scale dust storms, both in terms of frequency and season. If global-scale storms in MY 25 and 28 are removed, and we filter out single regional storms by averaging all years together, the annual distribution of CDOD looks like the one in Fig. 17. In this figure, the four distinct phases described above appear perfectly well defined. This figure represents an average climatological year, with departures from that characterizing the episodic regional storms. In each specific year the optical depth is locally modified (and the absolute value increased) by the onset and evolution of single dust storms, particularly in the second half of the year.

Fig. 18 summarizes the similarities and differences among the years. In panel (a) we show the time series of the values averaged in a 10° latitude band around the equator, whereas in panel (b) and (c) we plot the zonal means averaged over 10° solar longitude at two seasons (around the summer solstice and after the winter solstice). At equatorial latitudes (panel a), there is little interannual variability in northern spring/summer, and low CDOD. In these seasons, the gradient of CDOD increases moving towards northern high latitudes and southern mid-latitudes in TES years (panel b), whereas in MCS years the optical depth decreases to very low values at southern mid- and high latitudes. In the second half of the year (panel c), the background dust level shows remarkably little variability in the equatorial/tropical regions during the solsticial pause, except for the MY 28 year with a global-scale storm. Large CDOD gradients are again observed moving towards high latitudes in TES years, but not in MCS years. Outside the solsticial pause, dust storms (many of which are initiated by cross-equatorial flushing storms) produce peaks of CDOD in the equatorial region, which affect many longitudes. Panel (a) highlights the three equatorial phases for the dust distribution, already seen specifically for the locations of Gusev crater and Meridiani Planum in Fig. 13.

A feature that clearly stands out when looking at optical depths at high latitudes in the summer hemispheres and at polar cap edge latitudes in the winter hemispheres is that TES observes fairly high values near the polar cap edges, whereas little or no sign of such high values is present in the MCS observations. Very few THEMIS observations are available in MY 27 and 28, so it is difficult to judge these two years. There is, therefore, an apparent dichotomy between the TES years and the MCS years, which can be appreciated in panels (b) and (c) of Fig. 18, but also in the zonal means of Fig. 16. The dichotomy is particularly striking around the south polar cap edge after the (northern) summer solstice, when dust is likely to be lifted by southern baroclinic waves that are active at this season. In order to verify the presence or absence of dust storms at these latitudes, which could validate TES high optical depth values or MCS low values, we looked at orbital daily global mapping images taken by MOC and MARCI between $L_s = 80^\circ$ through $L_s = 130^\circ$ over multiple Mars years (MY 26–31), focusing along the south polar cap edge. Fig. 19 summarizes the results of the search for dust storms, showing that each Mars year – possibly with the exception of MY 25 – has at least one clear storm of 1000 km extension around the south polar cap edge. According

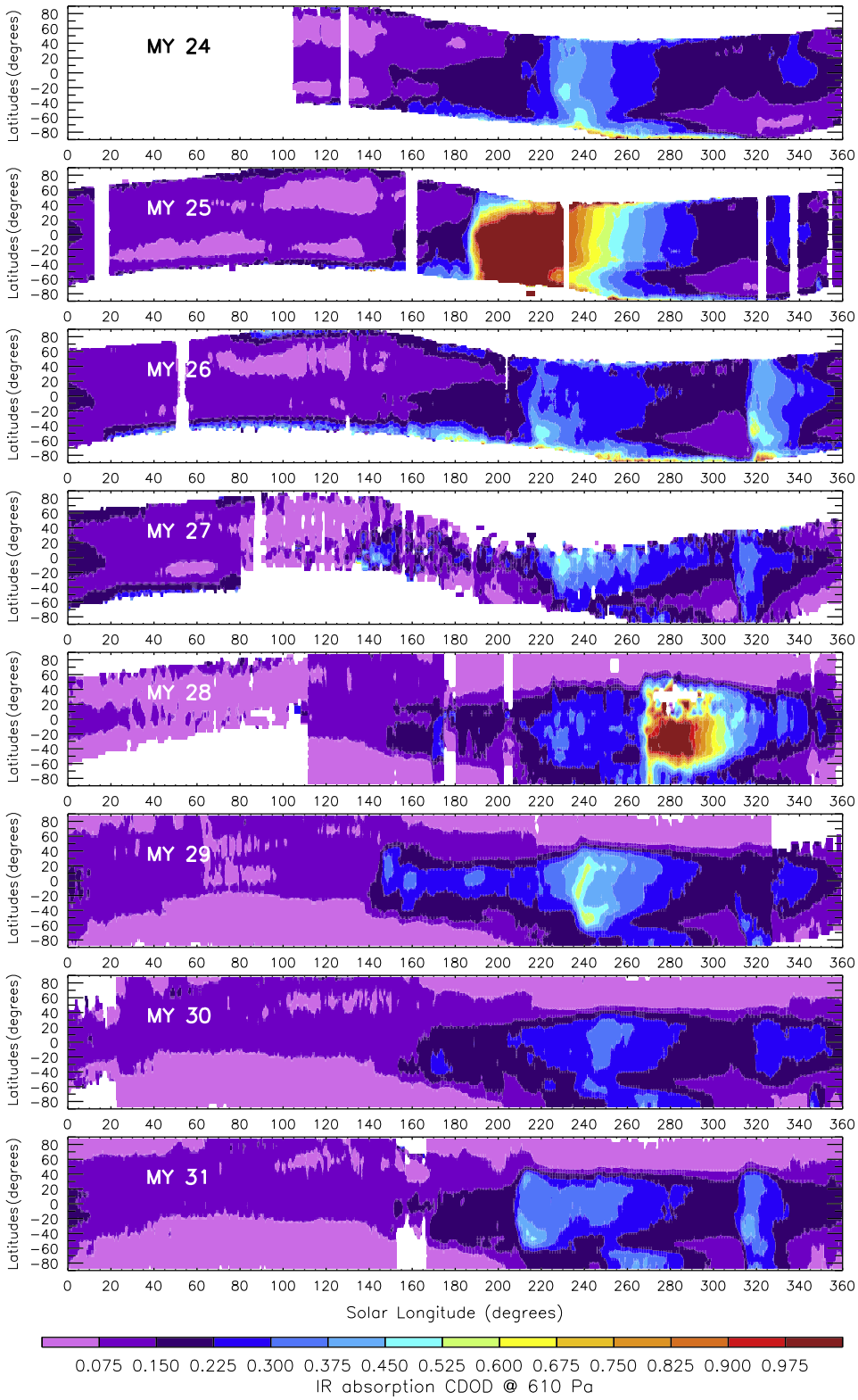

Fig. 16. Zonal means of 9.3 μm absorption column dust optical depth maps (normalized to 610 Pa), as a function of solar longitude and latitude for all eight available martian years. Data are extracted from the irregularly gridded maps obtained with the application of the IWB procedure.

to the definition by Cantor et al. (2001), based on area and duration, these storms are likely to be local. Moreover, the dust clouds appear mostly compact, which can be interpreted as the action of convective lifting with little diffusion by higher altitude winds. Preliminary GCM simulations with the GFDL Mars GCM show that dust, if lifted at these latitudes, is likely to be confined in the lower portion of the atmosphere – within the first kilometers – at this season by the descending branch of the Hadley circulation (not shown here). Under these circumstances, it is possible that MCS limb observations are not able to scan through these low atmospheric levels with such a small footprint, therefore missing the dust and detecting only very small values of opacity above

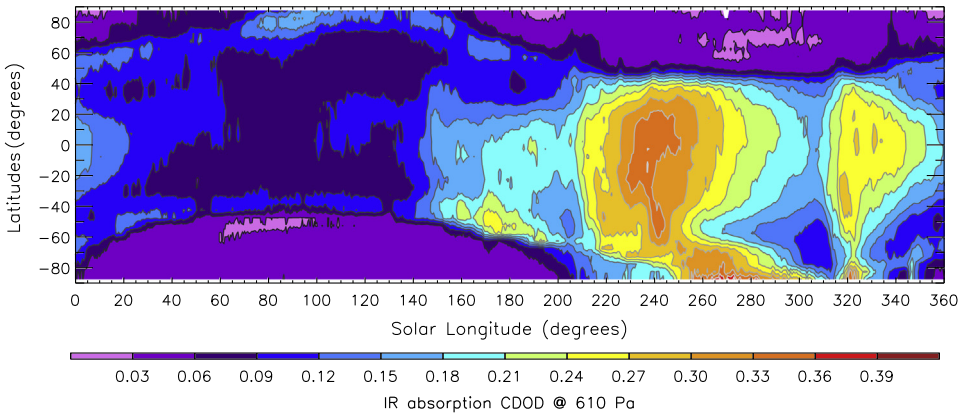

Fig. 17. Plot of the zonal mean of the 9.3 μm absorption column dust optical depth in the climatological year, as a function of solar longitude and latitude. The climatological year is obtained by averaging the irregularly gridded maps for all eight years, excluding the periods of planet-encircling dust storm activity in MY 25 and 28.

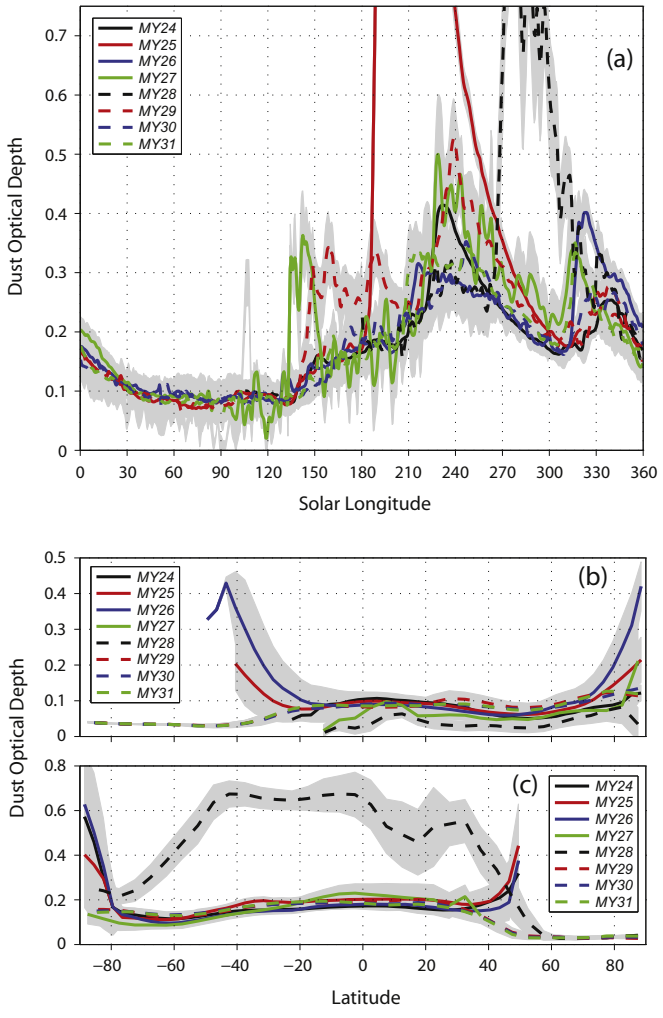

Fig. 18. Panel (a): Plot of equatorial (5°S–5°N) 9.3 μm absorption column dust optical depth normalized to 610 Pa (τ) as a function of solar longitude for all eight martian years, extracted from the gridded maps. Panel (b): Zonal mean of τ ($L_s = [95°, 105°]$) as a function of latitude for all eight martian years. Panel (c): Same as panel (b), but for the season $L_s = [295°, 305°]$.

the low dust layer at local scale. We also note that panels (a) and (d) of Fig. 15 suggest that dust lifted at high southern latitudes may not be well represented in the MCS opacity estimates at a later season. This hypothesis, though, does not exclude the possibility that TES retrievals of CDOD are overestimated around the cap edge, where the thermal contrast between the surface and atmosphere might be small. Retrievals in MY 26 and MY 27 are particularly suspicious, as the values of optical depth around the south cap edge are much higher than those measured in MY 24 and 25. Future retrievals of CDOD from MCS on-planet observations, or estimates from top-of-atmosphere brightness temperature fit, together with possible TES retrievals of CDOD over cold surfaces in the winter polar regions, might eventually provide insights into the correct dust distributions around the polar cap edges.

As an example of how our gridded products can be used to °explore the multiannual statistics of dust loading in particular regions, we consider the case of ESA's Exomars 2016 Entry, Descending and Landing Demostrator Module (EDM "Schiaparelli"). The landing is planned to take place in Meridiani Planum during the time window $L_s \sim 240$—$250°$ in MY 33, which is well inside the dust storm season. Although this will provide a unique opportunity to characterize a dust-loaded atmosphere during the entry, descending, and landing procedure, it will also pose strict constraints on the engineering parameters of the landing, and increase the associated risks. It is therefore very important to produce an accurate statistical prediction of the expected range of dust loading at the time and location of the landing, based on historical records. If one plots the time series of CDOD in all years in Meridiani, as in Fig. 18 (a), but limited to the period $L_s = 225°$–$265°$, the tail of the planetary-encircling dust storm stands out with respect to all other years, which show moderate dust loading (not shown here). It is worth noting that this season is characterized by the solsticial pause of the baroclinic wave activity, with associated lack of flushing storms, which in general have trajectories potentially affecting Meridiani. By calculating the average for the landing window $L_s = 240°$–$250°$ (at the nominal landing site in Meridiani (longitude 6.13°W, latitude 1.88°S)), we can make the statistical prediction, based on past observations, that Exomars 2016 "Schiaparelli" lander is likely to encounter a moderate dust loading with $\tau = 0.38 \pm 0.12$ (IR absorption normalized to 610 Pa). This prediction, though, does not exclude the possibility of high dust loading induced by an equinoctial planet-encircling dust storm, which, as mentioned above, can be quite unpredictable even just a few sols beforehand.

6. Building dust scenarios with kriging

With the application of the IWB procedure, the τ maps that we obtain are incomplete and have higher spatial resolution in MY 24,

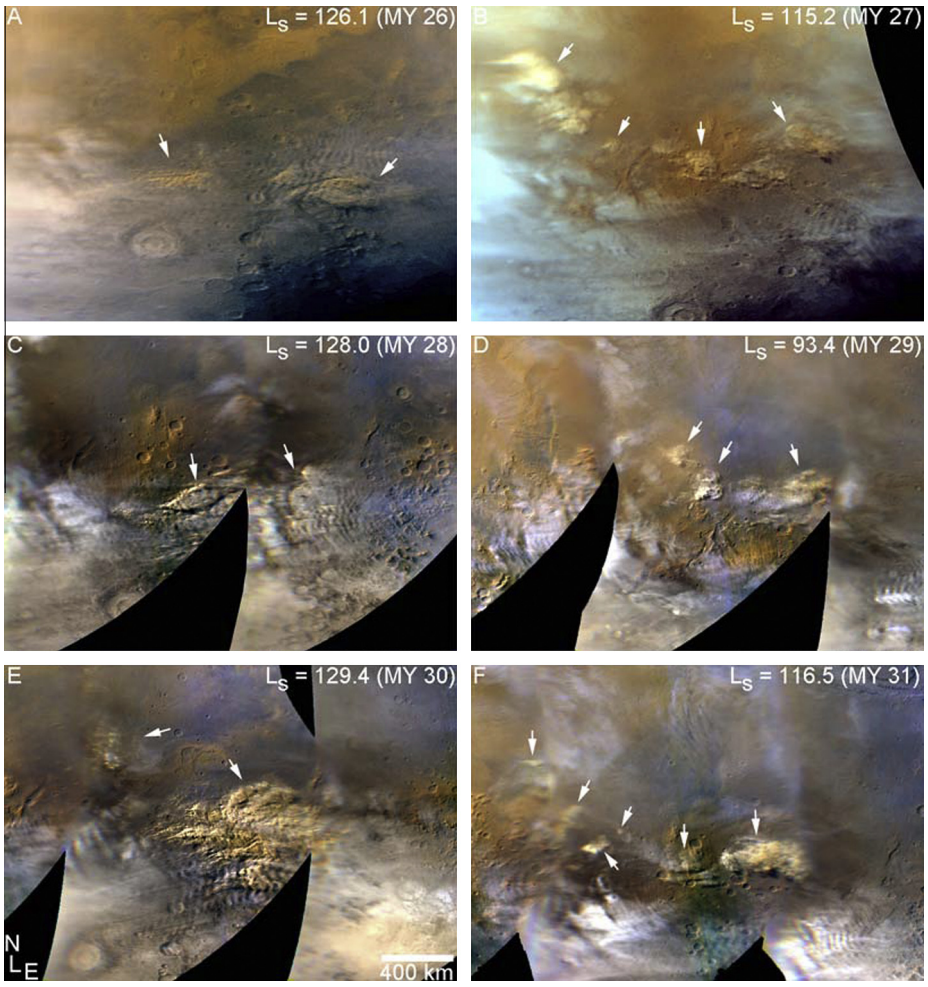

Fig. 19. Southern hemisphere dust storms close to the seasonal south polar cap edge observed between $L_s = 80^\circ$ through $L_s = 130^\circ$ over multiple Mars years (MY 26–31) from orbital daily global mapping images taken by: MGS-MOC on (A) January 21, 2003 at $L_s = 126.1^\circ$ (MY 26) and centered at 42.5°S, 67.0°W, (B) November 15, 2004 at $L_s = 115.2^\circ$ (MY 27) and centered at 35.5°S, 80.0°W, and by MRO-MARCI on (C) October 30, 2006, $L_s = 128.0^\circ$ (MY 28) and centered at 39.5°S, 7.0°W, (D) July 2, 2008, $L_s = 93.4^\circ$ (MY 29) and centered at 31.5°S, 89.0°W, (E) August 7, 2010, $L_s = 129.4^\circ$ (MY 30) and centered at 37.5°S, 64.0°W, and (F) May 27, 2012, $L_s = 116.5^\circ$ (MY 31) and centered at 28.0°S, 76.0°W. MARCI images are derived from the daily global map mosaics, while MOC images are single orbital passes. All images are simple cylindrically projections, mapped at a resolution of 3.75 km/pixel, spanning 50° of longitude and 35° of latitude. North is up and east is to the right. Local dust storms are indicated by a white arrow. Multiple arrows indicate multiple local storms. Condensate (water ice) clouds are also prevalent in all the images as diffuse white feature.

25, 26 than in the other years. For many practical applications it is desirable to have complete, regularly gridded maps spanning several years with the same resolution. One such application is to prescribe realistic aerosol dust distributions for global-scale or mesoscale climate model simulations (Greybush et al., 2012; Kavulich et al., 2013; Steele et al., 2014b). The production of the MCD statistics using the LMD GCM, for instance, is an obvious example (Millour et al., 2014). Other possible applications include the retrieval of surface or atmospheric variables using observations from which the aerosol dust component needs to be subtracted. Examples include retrieving atmospheric ozone (Clancy et al., 2014), surface albedo (Vincendon et al., 2014), and surface thermal inertia (Putzig and Mellon, 2007). For these reasons, in this Section we discuss our method to derive multiannual, regularly gridded 'dust scenarios' from the irregularly gridded maps we have described so far.

The process of producing complete gridded maps at a given resolution from maps that have missing data and different resolutions is, generally speaking, a problem of interpolation and/or extrapolation. There exist several techniques, each more or less 'optimal', to solve this problem, as it is the case for the gridding problem.

Kriging[3] is a technique that belongs to the family of linear least squares estimation algorithms. It is a method of interpolation that predicts unknown values from data provided at known locations. Unlike other common interpolation methods, such as polynomial, spline, and nearest-neighbor, kriging does not require an exact fit at each tabulated data point. Another important difference between kriging and other linear estimation methods is that kriging aims to minimize the error variance of the predicted values. Kriging applies a weighting to each of the tabulated data points based on spatial variance and trends among the points. Weights are computed by combining calculations of the spatial structure and dependence of the data, and building a statistical model of their spatial correlation (called a 'semivariogram' model). Alternatively, empirical semivariograms are often approximated by theoretical model functions, the most common of which are the spherical and the exponential semivariograms (we use the latter in this work). The reader can refer to Journel and Huijbregts (1978) for a general overview of the method. For the application of kriging to data gridding, Haylock

[3] The word 'kriging' is derived from the family name of Daniel G. Krige, whose Master thesis the French mathematician Georges Matheron used to develop the theory and formalism.

et al. (2008) provide an example for the case of temperature ground stations on the Earth, and Hofstra et al. (2008) evaluate kriging among other methods of spatial interpolation.

Given the spatial characteristics of the maps we have obtained after gridding the observations with the IWB procedure, kriging is the interpolation method that is likely to provide the best results, producing relatively smooth spatial variations even in cases when many missing values are present.

6.1. Pre-kriging modifications

Before applying the kriging to the maps, we have replaced some of the missing values using the following methods (in order of application).

1. In the TES, THEMIS and MCS datasets there are gaps in data coverage that sometime extend for few sols, e.g. during Mars solar conjunctions. In those cases, gridded maps are missing as well, if the gaps in data coverage are longer than 7 sols (the maximum TW we generally use). In addition, one or two daily maps before the first missing map and after the last missing map might have very few valid grid points in longitude. When long data gaps occur, we have increased the TW up to 25 sols, in order to accumulate enough observations to bypass the data coverage gap, and we have applied the gridding procedure again with more successive iterations. This method produces a smooth time interpolation by combining the moving average and the time weighting. In the absence of alternative information, or of a dynamical model of dust transport, this is a reasonable way to interpolate maps during periods of missing data.
2. Issues of data coverage are both temporal and spatial. The TES and THEMIS datasets have few valid retrievals of CDOD at high latitudes during the winter seasons, and the MCS dataset does not include estimates when the dust loading is too high (e.g. during dust storms), the water ice opacity is large (e.g. during the aphelion cloud tropical belt season), or the temperature at some height is below the CO_2 condensation temperature (e.g. during the polar nights, when CO_2 clouds might form). We can fill most of the spatial gaps in our gridded maps with general climatological values not representative of any specific year. To this purpose, for each sol-of-year we have calculated the average of all eight years (see Fig. 17 for a plot of its zonal mean), excluding the periods of planet-encircling dust storm activity in MY 25 and 28. By doing so, the influence of individual dust storms is mostly eliminated, and spatial inhomogeneities are smoothed out. However, the optical depths that result are underestimated with respect to any specific year, particularly in the dusty season. Before using an averaged map to fill gaps in the original gridded map at a specific sol-of-year, therefore, we have to re-normalize the averaged values to a level consistent with a representative dust optical depth for that sol. To this purpose, for each sol in MY 27–31 we can use independent observations of optical depth by PanCam 'Spirit' and PanCam 'Opportunity' to calculate normalization factors. We actually use the minimum between the sol-averaged observations from Spirit and Opportunity, after having interpolated the time series to fill any possible gap. The use of the minimum value avoids re-normalizing the averaged maps with values characteristic of specific dust storms located at either Spirit's or Opportunity's site. Furthermore, it is consistent with satellite observations in northern summer (see Section 4), so that we avoid biases in the re-normalization. For an average map at a given sol-of-year, we calculate the mean τ_{ave} in a latitude band $[-15^\circ, 0^\circ]$ (we recall that the locations of Spirit and Opportunity are, respectively, close to -14° and -2° latitude), and we re-normalize the values of this map by multiplying by the following function ν:

$$\nu = \begin{cases} r_\tau + \frac{1-r_\tau}{2}\left(1 - \tanh\frac{\theta+45^\circ}{12^\circ}\right) & \text{if } \theta < 0^\circ \quad \text{(a)} \\ r_\tau + \frac{1-r_\tau}{2}\left(1 + \tanh\frac{\theta-45^\circ}{12^\circ}\right) & \text{if } \theta > 0^\circ \quad \text{(b)} \end{cases} \tag{11}$$

where θ is the latitude, and $r_\tau = \tau_{MER}/\tau_{ave}$ (τ_{MER} is converted to equivalent IR absorption by dividing by 2.6). We replace a missing grid point in a gridded map at a given sol-of-year in MY 27–31 with the corresponding value from the averaged map, multiplied by ν, if a particular condition is satisfied. The condition is that the distance between the missing grid point and the closest valid grid point must be greater than a certain threshold distance, set equal to 1000 km. The threshold avoids the introduction of possible artificial discontinuities between valid gridded values and filled values in the maps.
3. No valid grid points exist at very high latitudes during the polar winters in TES MY 24–26. In order to constrain the kriging interpolation at high latitudes and at the poles in these years, we replace the value of the missing grid points located 15° poleward of the northernmost or southernmost valid latitude with the corresponding value from the climatologically averaged map at the given sol-of-year. No normalization is applied in this case, because no independent observations of optical depth exist. This approach, although arbitrary, is consistent with estimated optical depths by MCS in the polar regions and with the reduced weight of the normalization function at high latitudes, according to Eq. (11). It may be revised in future updates of the dust scenarios, if new TES retrievals in the polar regions become available.

We described in Section 5 the observed difference between TES and MCS values of optical depth around the polar cap edges. No conclusive evidence exists at the time of writing to favor either set of observations, only circumstantial evidence points towards the possibility that MCS underestimates the opacity when the lifted dust is confined to low altitudes. This dichotomy between MY 24, 25, 26 and 27 from one side, and MY 28, 29, 30, 31 on the other is most likely not realistic. We have therefore decided to modify the values of optical depth around the polar cap edge in all years, to minimize the TES-MCS questionable variability in the dust scenarios. In the v2.0 scenarios, we have limited the modification to the south cap edge in the solar longitude range $L_s = [0^\circ, 205^\circ]$ (except for MY 25 where we limit the range to $L_s = 180^\circ$ to preserve the planet-encircling storm). To this purpose, for each sol within this range we use the averaged year as in Fig. 17 to calculate a mean value τ_{ave} in a 30° latitude band centered around the latitude of the south polar cap edge. We use data from Piqueux et al. (2015a) to interpolate the cap edge latitude at the necessary sol-of-year. We calculate the mean value τ_{grid} in the same latitude band for each corresponding gridded map, and we take the ratio of the two values $r_\tau = \tau_{ave}/\tau_{grid}$. For a gridded map (of any year) within the defined range of solar longitudes, and for southern latitudes $\theta < 0^\circ$, we multiply the τ values by the following function:

$$\mu = 1 + (r_\tau - 1)\exp\left(-\frac{(\theta - \theta_{cap})^2}{2\sigma^2}\right), \tag{12}$$

where θ_{cap} is the interpolated latitude of the cap edge, and $\sigma = 15^\circ$. The effect is that large optical depth values at the edge of the south polar cap in TES years tend to decrease, the closer to the cap edge. On the contrary, small values in MCS years tend to increase. Overall, optical depths near the south cap edge in northern spring/summer converge to climatological values within a latitude band. The same procedure could in principle be applied to other seasons and to the north polar cap. We reserve the possibility of extending it in future versions of the dust scenarios, if a proper solution of the TES-MCS apparent difference at the edge of the polar caps is not found.

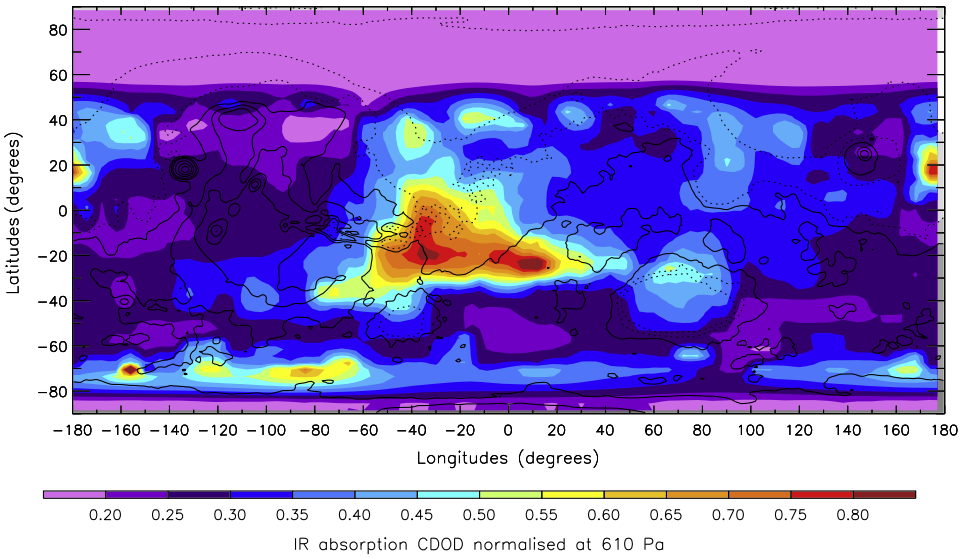

Fig. 20. Map of 9.3 μm absorption column dust optical depth corresponding to Fig. 6 (sol-of-year 449, MY 24) after the application of kriging. The map is regular and complete, on a $3^\circ \times 3^\circ$ longitude-latitude grid.

6.2. Interpolation by kriging

After replacing missing values in the incomplete gridded maps, and modifying the south polar cap edge values, the data fields are ready to be interpolated by kriging.

We have used the IDL v8.3 built-in routine GRIDDATA for kriging interpolation on the sphere with an exponential semivariogram model set by default (nugget, sill, and range parameters are those proposed by the IDL routine). We have chosen a fairly high resolution grid of $3^\circ \times 3^\circ$ in longitude-latitude, uniform for all years. At the end of the interpolation procedure, carried out for each available sol from MY 24 to MY 31, we obtain complete, regularly gridded maps of IR absorption CDOD normalized to 610 Pa Note that there are no observations for the first part of MY 24 (before sol-of-year 225), therefore we use MY 25 and 26 to fill the gap, as explained in Appendix B. Fig. 20 shows a kriged map as an example based on the same sol-of-year as in Fig. 6.

Similarly to what we do for the irregularly gridded maps, we provide an animation of the daily dust scenario maps as supplementary material of this paper. The structure of the animation is the same: 669 frames (one per sol-of-year), each one having eight maps for the respective years. The dust scenarios (currently 2.0) can be downloaded from the same URL in NetCDF format. Fig. 21 shows zonal means built from the dust scenario maps as a function of solar longitude and latitude, as in Fig. 16 for the irregularly gridded maps.

7. Summary and future developments

In this paper we have described the procedures to obtain daily gridded maps of column dust optical depth for eight martian years, from $L_s \sim 105^\circ$ in MY 24 to the end of MY 31. We have used retrieved and estimated CDODs from three different instruments (TES, THEMIS, and MCS) aboard different polar orbiting satellites (MGS, ODY, and MRO). Data have been collected for about 14 Earth years of spacecraft missions, from 1999 to 2013.

Observed CDODs have been firstly gridded using the IWB methodology, which produces daily maps on a regularly distributed grid, but with missing values at some grid points. Subsequently, these incomplete maps have been interpolated onto a regular grid, using the kriging method, after the application of a series of procedures to replace most of the missing values with climatological values. The two datasets of IR absorption CDOD normalized to the reference pressure of 610 Pa (irregularly gridded maps and regularly kriged ones) have been separated in martian years, and made publicly available in NetCDF format on the MCD project website, hosted by the LMD (URL: http://www-mars.lmd.jussieu.fr/). Two animations of the current version 2.0 of the maps are also available as supplementary material to this paper.

The key achievements of this work are the production and analysis of a continuous, multiannual climatology of dust based on several heterogeneous datasets, as well as the assessment of uncertainties and biases, both in the CDOD retrievals and in the resulting gridded maps. Eight martian years of temporal and spatial (2D) dust distribution have been presented in terms of interannual and interseasonal variability, down to the daily evolution of individual dust storms. We have confirmed that the years without global-scale storms are characterized by four phases in the solar longitude-latitude dust distribution, clearly highlighted in panel (a) of Fig. 18 and in Fig. 17. Our results are consistent with the analysis of pre- and post-solstice storms discussed by Wang and Richardson (2015), Kass et al. (2014). The time series of dust optical depth is consistent with that of mid-atmosphere temperatures (Kass et al., 2014). We have carried out an extensive validation of the gridded maps using independent observations (PanCam, Mini-TES, SSI, CRISM, MOC and MARCI), and we have confirmed or newly discovered a few important biases, which point to instrumental biases rather than errors in the gridding procedure. Three biases in particular should be addressed by future analysis:

- Mini-TES and PanCam in Meridiani Planum observe much larger optical depths than satellite instruments in spring and summer, although smaller biases are present at other seasons in the available time series.
- CRISM observes much larger optical depths than MCS overall, without clear patterns in latitude or solar longitude.
- TES and MCS observe very different optical depths near the polar cap edges. TES generally provides a sharp latitudinal increase in optical depth when approaching both the north and south cap edges, whereas MCS suggests very low values.

A fourth bias is related to THEMIS, which generally observes dust optical depths lower than TES and MCS in the first half of each martian year (as shown in the zonal means obtained by gridding only THEMIS observations, and provided as supplementary

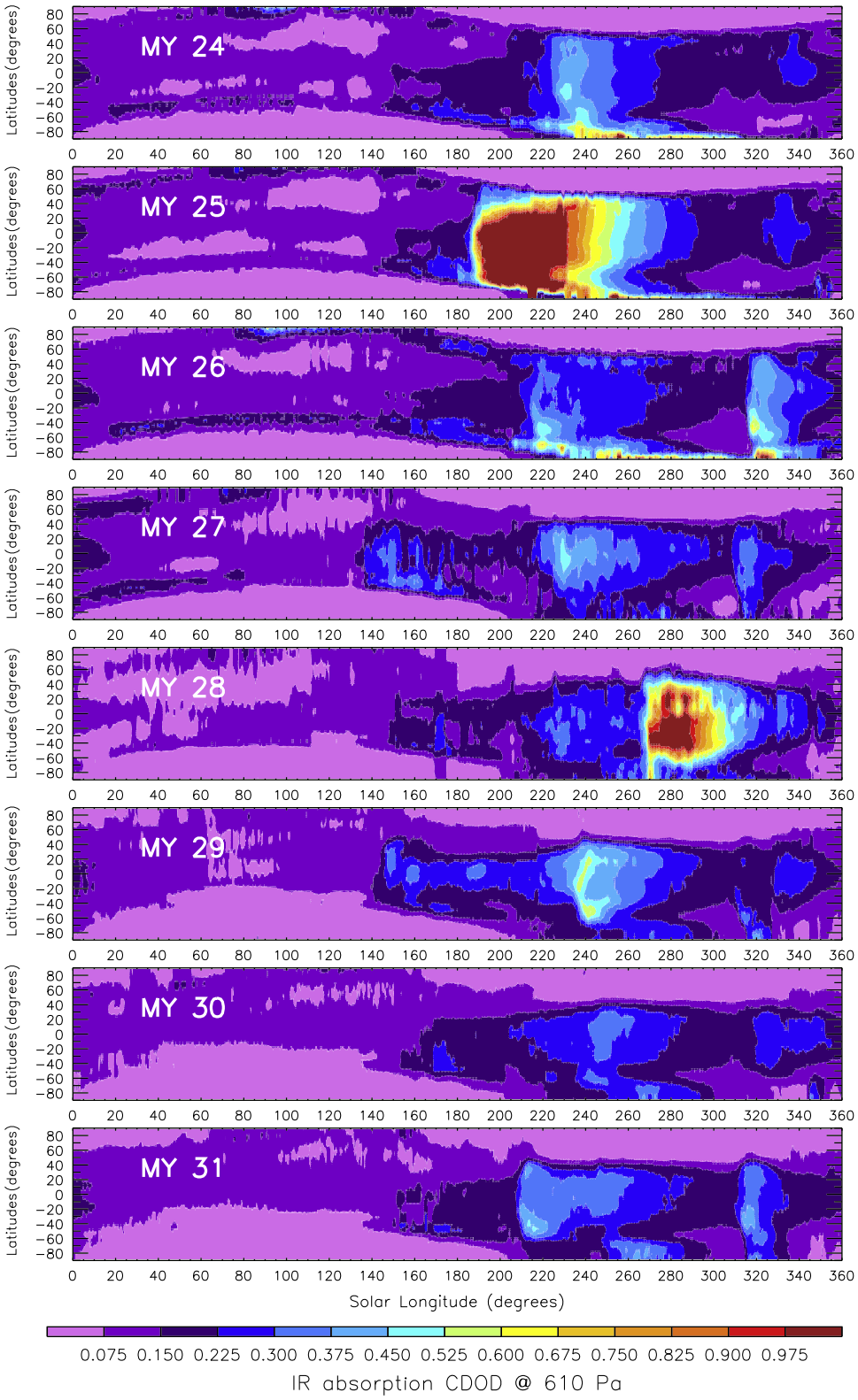

Fig. 21. Zonal means of 9.3 μm absorption column dust optical depth maps (normalized to 610 Pa) as a function of solar longitude and latitude for all eight available martian years, calculated using the regularly gridded maps after the application of the kriging procedure.

material of this paper). Some of these biases may be related to the role played by water ice clouds. We have extensively discussed the effect of clouds in PanCam as well as in MCS observations. Water ice and dust cannot be distinguished by ground-based cameras, and are more difficult to distinguish by ground-based spectrometers like Mini-TES, which might explain larger than expected opacities observed during the aphelion season. In the same season, MCS dayside profiles of opacities are limited by the large amount

of water ice aerosols, preventing reliable extrapolations of dust opacity to low altitudes. On the other hand, both TES and THEMIS have sufficient spectral coverage and resolution to easily separate the spectral signatures of dust and water ice aerosols, which should prevent confusion between the two aerosols. Overall, it is very difficult to definitively assess which instrument is more reliable or which portion of the interannual variability is instrumentally-driven. We have nevertheless provided some hints in this paper, and we have demonstrated that camera images such as those provided by MOC and MARCI, combined with gridded maps, can certainly help to provide a reliable and quantitative approach to the study of the dust interannual variability. The use of GCM simulations (possibly associated with data assimilation techniques) has the potential to add a further level of information.

Future developments of this work will include the update of the climatology with the addition of new and/or re-processed retrievals, not only for martian years beyond MY 31, but also for those already described in this paper. The MCS team expects to carry out retrievals of CDOD (as additional standard product) using nadir and off-nadir observations, which would greatly improve the quality of the dataset and reduce the biases identified in this work. The use of estimated CDODs from fitting top-of-atmosphere brightness temperatures with a GCM can be another important source of information to be used in the gridding procedure, in order to increase the number of observations (particularly dayside observations) and reduce the uncertainties in some areas. This is illustrated in panels (b) and (d) of Fig. 15, and should provide improved opacity estimates in cases where the current extrapolation of MCS opacity profiles is unreliable (due to the failure of the retrieval at low-altitude). In anticipation of future developments, we show in Fig. 22 the zonal mean of available MY 32 gridded maps as a function of solar longitude and latitude. To produce this figure we have gridded available MCS observations until the end of December 2014 using the IWB methodology. The plot shows low dust optical depth values consistent with previous years in spring and summer (as expected), a seasonal increase of optical depth after the autumn equinox, and a rapid increase after $L_s = 215^\circ$. This rapid increase (up to $\tau \sim 0.8$) is due to the development of a regional storm in Hesperia Planum (between the northern rim of Hellas and Isidis Planitia), which moved westward while increasing in size, opposite to what a similar storm in this location did in MY 25 (at $L_s = 186^\circ$) at the onset of the planet-encircling dust storm. This latest example illustrates how important a reliable, complete, long-term, quantitative dust climatology is to study the variability of the dust storms on Mars and, ultimately, to try and forecast their onset.

New observations are paramount to this purpose. Reliable retrievals of CDOD from the Planetary Fourier Spectrometer (PFS) observations aboard Mars Express, for instance, would be invaluable in improving the quality of the maps in MY 27 and MY 28, when only sparse THEMIS observations are available. The IWB procedure would be particularly adapted to grid PFS observations, which are fairly heterogeneous in local time, possibly using time resolutions of a fraction of a sol. Finally, a time resolution of half a sol would provide insights into the diurnal variability of the optical depth, if both dayside and nightside observations were fully used. MCS dayside observations would require careful filtering to avoid large extrapolations, or, alternatively, dayside estimates of dust optical depth from fitting top-of-atmosphere brightness temperatures with a GCM could provide the necessary dataset to be gridded. Recent retrievals of TES nightside CDOD by Pankine et al. (2013) can be integrated in future versions of our gridded and kriged products.

The use of data assimilation with an aerosol transport model (if not with a dynamical model of the dust cycle) would be an obvious improvement of the simple spatial kriging used in this work to produce complete dust scenarios, with ensemble methods providing the capability to estimate uncertainties. Work in this direction has been done by Greybush et al. (2012), Steele et al. (2014a,b), Navarro et al. (2014), after a first attempt by Montabone et al. (2006) to assimilate dust optical depths in a GCM without explicitly using an aerosol transport model. Despite the possible use of data assimilation techniques as 'optimal interpolators' of dust observations (or other types of aerosols and variables), gridding retrievals from satellite orbits with the IWB procedure can retain its key advantages of (1) being easy to implement, (2) not requiring a model, (3) providing statistical estimates of uncertainties based on those of the retrievals, and (4) giving immediate access to statistical analysis of the spatio-temporal evolution of events. Furthermore, this gridding technique could be applied to fields beyond the study of the martian dust climatology, where data assimilation techniques might not be accessible or might be more difficult to implement.

Acknowledgments

The work published in this paper was funded by contracts with the European Space Agency to develop the Mars Climate Database. LM also acknowledges funding from the French Centre National de la Recherche Scientifique (CNRS) and the American National Aeronautics and Space Administration (NASA) under grant no. NNX13AK02G issued through the Mars Data Analysis Program 2012. The authors are indebted to many people whose direct or indirect help made it possible to write this paper. A particular mention is due to Aymeric Spiga, who always believed this paper would be finished one day, and provided time and competence during long discussion sessions. LM is grateful to Mathieu Vincendon, Joachim Audouard, Tanguy Bertrand, Frank Daerden, Melinda Kahre, and Daniel Tyler Jr. for feedback on earlier versions of the dust scenario maps, and to Helen Wang for initially guiding us through the MARCI images. We are also particularly grateful to Mathieu Vincendon and another anonymous reviewer for their comments and suggestions, which greatly helped to improve the paper. Last but not the least, LM wishes to thank his wife, Héloïse, for accepting the loss of many days of vacation during the long period he worked on this paper, and his newborn daughter, Lara, for having given him a good reason to speed up the writing!

Appendix A. A sol-based martian calendar

A martian year has 668.5921 mean solar days (sols) or, with good approximation, 668.6 sols. The solar longitude resets to zero by definition at the beginning of each new year (spring equinox).

The scientific community primarily have been using a martian calendar based on the combination of martian year and solar longitude, since data are usually averaged over a few solar longitude degrees. This combination is not satisfactory in our work, because our series of maps uses the sol as time variable[4]. If we want to devise a martian calendar based on sols, we need to keep track of the fraction of a sol left at the end of each martian year, similarly to what is done for the Earth calendar. Many sol-based calendars have been proposed for Mars, with different solutions for the structure of months and weeks, and for the way they deal with the leap years. We mention here only the example of the Darian calendar (first described in a paper published by Gangale, 1986), which has been proposed to serve the needs of possible future human settlers on Mars.

[4] More specifically, the independent time variable we use is the fractional sol since the beginning of a martian year (marked by sol = 0.0). A sol starts at 00:00 MUT and ends at 24:00 MUT. The .5 fraction corresponds to 12:00 MUT. We also define the sol-of-year variable, which is the integer sol number starting from sol 1 as first sol of the year.

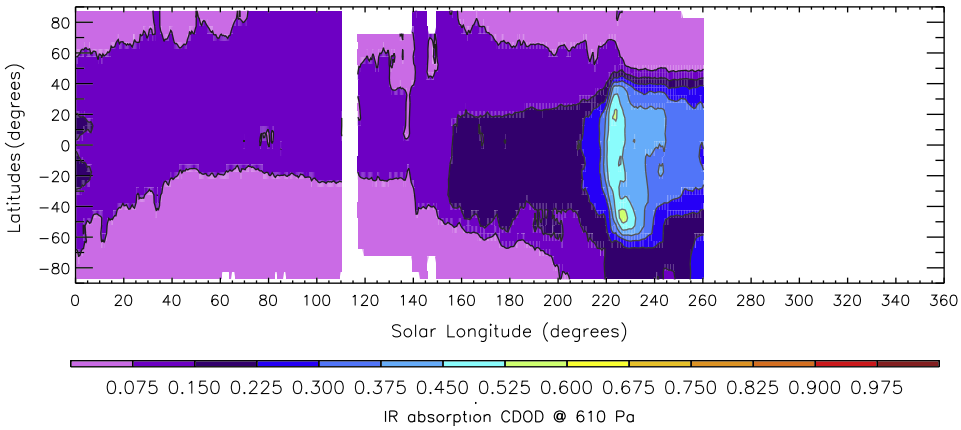

Fig. 22. Zonal means of gridded maps of 9.3 μm absorption column dust optical depth (normalized to 610 Pa) as a function of solar longitude and latitude in MY 32. The gridded maps use only MCS estimates from July 31, 2013 until the end of December 2014.

For scientific purposes, and in the interest of simple time-keeping, we have devised for the present work our own sol-based martian calendar. Since there are approximately 668.6 sols in a martian year, every 5 years the number of elapsed sols is very close to the integer 3343. It is convenient, therefore, to define cycles of 5 martian years, with a number of sols respectively of 669.0, 668.0, 669.0, 668.0, and 669.0 (a total of 3343 sols). By doing so, the end of each cycle is (without approximation) only 0.04 sol shorter than an integer number of sols, which accumulates to 1/4 of a sol after 30 martian years (a reasonable amount for scientific purposes). Furthermore, assuming the first sol of a year starts when it is midnight at the prime meridian (00:00 MUT), if there is a time bias t_b between sol = 0.0 and $L_s = 0^\circ$ at the beginning of a 5-year cycle, there is again the same bias at the beginning of the following cycle, if we approximate the martian year with 668.6 sols. Thanks to this property, the time biases between our sol-based calendar and a solar longitude-based calendar follow a repeatable pattern, and they are never too large for a reasonable number of martian years, if t_b is properly set at the beginning of MY 1.

Clancy et al. (2000) proposed an arbitrary convention to numerate the martian years starting from April 11, 1955 at 08:31 UTC (MY 1, $L_s = 0^\circ$). This date corresponds to the martian northern spring equinox preceding the planet-encircling dust storm of 1956. This storm marks the beginning of the new period of systematic observation and exploration of the planet Mars. Using this convention (adopted by most of the scientific papers about Mars since its introduction), all scientific data can be easily compared using a calendar based on positive martian years (see Piqueux et al., 2015b, for an extension to negative martian years). For a solar longitude-based calendar, every new martian year since this date is marked by the occurrence of the northern hemisphere spring equinox.

For the sol-based calendar introduced in the present paper, we maintain the numeration of the martian year introduced by Clancy et al. (2000), but we have to start our MY 1 at a slightly different time, because at $L_s = 0^\circ$ in MY 1 the MUT time (local mean solar time) was 13:26[5] rather than 00:00 h. The first sol of MY 1 in our calendar starts on April 11, 1955 at 19:22 UTC, when it was $L_s = 0.2^\circ$ and 00:00 MUT on Mars, i.e. $t_b = 0.44$ sol. By the beginning of MY 26, this bias has reduced to $t_b = 0.24$, therefore the sol-based calendar we use is less than 6 h late with respect to the calendar based on solar longitude at the spring equinox of MY 26, and less than 5 h late at the beginning of MY 31 (i.e the beginning of the following 5-year cycle). This bias is satisfactory for the climatology from MY 24 to MY 31, and we make the approximation that $t_b = 0.24$ sol (0.12° solar longitude) for the three cycles we deal with in this paper. By doing so, we can easily subtract a constant offset at the new year's sol in MY 21, 26 and 31, to find the solar longitude of the corresponding spring equinox, with an error of about one hour in MY 21 and 31 with respect to MY 26. In Table 2, we summarize the number of sols for each martian year and the solar longitude corresponding to each new year's sol.

Table 2
The sol-based martian calendar used in the present work. MY 1 new year's sol (00:00 MUT) is on April 11, 1955 at 19:22 UTC.

5-year cycle number	martian year	Number of sols	New year's solar longitude
5	24	668	359.98
5	25	669	359.67
6	26	669	359.88
6	27	668	0.08
6	28	669	359.78
6	29	668	359.98
6	30	669	359.67
7	31	669	359.88

Appendix B. Description of the (irregularly) gridded CDOD dataset and dust scenarios, v2.0

The parameters specifically used for the IWB procedure to produce the eight-year irregularly gridded CDOD dataset version 2.0 are summarized in Table 1.

The eight NetCDF[6] files of the gridded dataset (one for each available martian year) can be downloaded from the MCD website hosted by the LMD at the URL: http://www-mars.lmd.jussieu.fr/.

Each file includes variables depending on three possible dimensions: longitude, latitude, and time. Longitudes are east longitudes in the range $[-180^\circ, 180^\circ]$, latitudes are in the range $[90^\circ, -90^\circ]$. The spatial resolution is $6^\circ \times 3^\circ$ longitude × latitude for MY 24, 25, and 26, $6^\circ \times 5^\circ$ longitude × latitude for the other years. The time variable (fractional sol) is either in the range [0.5, 667.5] or [0.5, 668.5], depending on the year (see Table 2), with time resolution of 1 sol. Non-valid grid points are assigned a Not-a-Number (NaN) value.

Included one-dimensional variables are longitude(longitude), latitude(latitude), time(time), sol-of-year(time), and L_s(time).

[5] All times are calculated using the NASA-GISS Mars24 applet, http://www.giss.nasa.gov/tools/mars24/.

[6] See http://www.unidata.ucar.edu/software/netcdf/index.html for details on the NetCDF data file format.

Three-dimensional variables (all depending on longitude, latitude, time) are:

- cdodnum: The number of averaged observations at the corresponding valid grid point.
- cdodtw: The minimum time window for a valid grid point (e.g. a value 3 means observations have been averaged within three sols to provide a valid τ at the grid point).
- cdodrel: The reliability value of the grid point, calculated as the weighted average of the reliability values of the single observations. It is worth noting that, for the way reliability has been defined (see Section 2.4 and related Section 2.3), there are no single reliability values lower than 0.6, therefore values of cdodrel are $\geqslant 0.6$.
- cdod610: The column dust optical depth in absorption at 9.3 μm, normalized to the reference pressure of 610 Pa.
- cdod610unc: The combined uncertainty of the column dust optical depth normalized to 610 Pa (see Eq. (5)).
- cdod610rmsd: The root mean squared difference of the column dust optical depth normalized to 610 Pa (see Eq. (4)).
- cdodtot: The column dust optical depth in absorption at 9.3 μm, provided at the average grid point surface pressure.
- cdodtotunc: The combined uncertainty of the column dust optical depth in absorption at 9.3 μm, provided at the average grid point surface pressure.

While the cdod610 variable and its related uncertainty refer to the τ variable described in Section 3.2 and following sections (i.e. normalized to 610 Pa), the cdodtot variable and its uncertainty included in the dataset refer to the non-normalized, total optical depth, i.e. the optical depth of the entire atmospheric column down to the local surface. Obviously, we can only provide an estimate of such a variable, as the IWB procedure requires the calculation of averages using uniform values (i.e. normalized to the surface pressure). For each grid point k, we calculate a weighted average (PS_k) of the surface pressure of the n observations (ps_n), using the same IWB procedure and parameters as for the dust. The surface pressure and its uncertainty for each observation are extracted from the MCD using the `PRESO` routine. We then divide cdod610 by 610 Pa and multiply by PS_k at each grid point. The variable we obtain is a consistent estimate of the total optical depth. The combined uncertainty is calculated by propagating the uncertainties on cdod610 and PS_k. Note that one can calculate the irregularly gridded surface pressure field as $PS = (\text{cdodtot}/\text{cdod610}) \cdot 610$.

The eight NetCDF files of the kriged dataset v2.0 can also be downloaded from the MCD website at the same URL. The spatial resolution is fixed to $3^\circ \times 3^\circ$ in longitude and latitude, and the number of sols is fixed to 669 in each year (the time variable is in the range [0.5, 668.5]). The reason for this choice is that atmospheric models using dust scenarios are often based on a fixed number of sols per year. For years with 668 sols in our sol-based martian calendar, we add the first sol of the following year. The sol-of-year 669 in MY 24, 27, 29, therefore is the same as the sol-of-year 1 in, respectively, MY 25, 28, and 30. In other words, the scenarios smoothly wrap from year to year. Since there are no maps available for the first part of MY 24 (before sol-of-year 225), we use the average of the first 224 sols of MY 25 and 26 to fill the gap, therefore creating a hybrid TES MY 24 year. We prefer to not use MY 27 in the average because the quality of TES observations in MY 27 is possibly degraded. The junction at sol-of-year 225 is smoothed using a running average for the three sols before and the three sols after. It is worth mentioning that if one wants to use a scenario for a specific year in a cyclic model simulation, the first few sols and the last few sols should be averaged (e.g. with a running average) to avoid the discontinuity between the beginning and the end of the year.

The dust scenarios include the same dimensions and one-dimensional variables as the irregularly gridded dataset. As for the three dimensional variables, they include:

- cdodrel: The reliability value of the grid point, interpolated with kriging from the irregularly gridded dataset.
- cdod610: The column dust optical depth in absorption at 9.3 μm, normalized to the reference pressure of 610 Pa, interpolated with kriging from the irregularly gridded dataset.
- cdodtot: The column dust optical depth in absorption at 9.3 μm, provided to the interpolated surface pressure.

In order to calculate the total optical depth in the case of the kriged maps, we divide the interpolated cdod610 by 610 Pa and we multiply by the surface pressure value interpolated from the gridded dataset. Note that, before interpolating, we replace the missing surface pressure values with climatological values extracted from the MCD (representing the average of 9 locations per grid point).

Combined uncertainties and RMSD values are not provided in the dust scenarios files, because by using a default IDL routine we cannot derive an uncertainty from the interpolation procedure itself, and because it would be totally arbitrary to assign uncertainties to the modified or replaced grid points described in Section 6.1, before the application of the kriging. In contrast, we interpolate the reliability value, which can be used as an estimate of the quality of a grid point. Before the application of the kriging interpolation, we assign specific reliability values to missing or special grid points, so that one can distinguish areas of the kriged maps where values were modified with respect to the original maps gridded with IWB. In particular, we assign 0.3 to grid points where optical depth values are provided by climatological values (including all grid points for sol-of-year < 225 in MY 24); 0.4 to missing grid points; 0.5 to modified grid points around the southern polar cap edge, and to grid points where cdodtw > 15 sol; 0.6 to grid points where $7 <$ cdodtw ≤ 15.

Appendix C. Supplementary material

Supplementary data associated with this article can be found, in the online version, at http://dx.doi.org/10.1016/j.icarus.2014.12.034.

References

Basu, S. et al., 2006. Simulation of spontaneous and variable global dust storms with the GFDL Mars GCM. J. Geophys. Res. 111, E09004.
Bell III, J.F. et al., 2003. Mars Exploration Rover Athena Panoramic Camera (PanCam) investigation. J. Geophys. Res. 108, 8063. http://dx.doi.org/10.1029/2003JE002070.
Bell III, J.F. et al., 2009. Mars Reconnaissance Orbiter Mars Color Imager (MARCI): Instrument description, calibration, and performance. J. Geophys. Res. 114, E08S92. http://dx.doi.org/10.1029/2008JE003315.
Cantor, B.A., 2007. MOC observations of the 2001 Mars planet-encircling dust storm. Icarus 186, 60–96.
Cantor, B.A. et al., 2001. Martian dust storms: 1999 Mars Orbiter Camera observations. J. Geophys. Res. 106 (E10), 23653–23687.
Christensen, P.R. et al., 2001. Mars Global Surveyor Thermal Emission Spectrometer experiment: Investigation description and surface science results. J. Geophys. Res. 106, 23,823–23,871.
Christensen, P.R. et al., 2004. The Thermal Emission Imaging System (THEMIS) for the Mars 2001 Odyssey mission. Space Sci. Rev. 110, 85–130.
Christensen, P.R. et al., 2003. Miniature thermal emission spectrometer for the Mars Exploration rovers. J. Geophys. Res. (Planets) 108, 8064. http://dx.doi.org/10.1029/2003JE002117.
Clancy, R.T. et al., 2000. An intercomparison of ground-based millimiter, MGS TES, and Viking atmospheric temperature measurements: Seasonal and interannual variability of temperatures and dust loading in the global Mars atmosphere. J. Geophys. Res. 105, 9553–9571.

Clancy, R.T., Wolff, M.J., Christensen, P.R., 2003. Mars aerosol studies with the MGS TES emission phase function observations: Optical depths, particle sizes, and ice cloud types versus latitude and solar longitude. J. Geophys. Res. 108 (E9). http://dx.doi.org/10.1029/2003JE002058.
Clancy, R.T., et al., 2014. MARCI Global Daily Ozone Mapping and Comparison to LMD GCM Simulations: Polar Dynamics, Hellas Basin, and Heterogeous Chemistry. In: Proceedings of the Fifth International Workshop on the Mars Atmosphere: Modelling and Observation, 13–16 January, Oxford, UK.
Fenton, L.K., Pearl, J.C., Martin, T.Z., 1997. Mapping Mariner 9 dust opacities. Icarus 130, 115–124.
Forget, F. et al., 1999. Improved general circulation models of the martian atmosphere from the surface to above 80 km. J. Geophys. Res. 104, 24155–24176.
Gangale, T., 1986. martian standard time. J. Brit. Inter. Soc. 39 (6), 282–288.
Greybush, S.J. et al., 2012. Ensemble Kalman filter data assimilation of thermal emission spectrometer (TES) profiles into a Mars global circulation model. J. Geophys. Res. Planets 117, E11008. http://dx.doi.org/10.1029/2012JE004097.
Grotzinger, J.P. et al., 2012. Mars Science Laboratory Mission and Science investigation. Space Sci. Rev. 170 (1–4), 5–56.
Guzewich, S.D. et al., 2013a. High-altitude dust layers on Mars: Observations with the Thermal Emission Spectrometer. J. Geophys. Res. 118 (6), 1177–1194.
Guzewich, S.D. et al., 2013b. The impact of a realistic vertical dust distribution on the simulation of the martian General Circulation. J. Geophys. Res. 118 (5), 980–993.
Haylock, M.R. et al., 2008. A European daily high-resolution gridded data set of surface temperature and precipitation for 1950–2006. J. Geophys. Res. 113, D20119. http://dx.doi.org/10.1029/2008JD010201.
Hofstra, N. et al., 2008. Comparison of six methods for the interpolation of daily European climate data. J. Geophys. Res. 113, D21. http://dx.doi.org/10.1029/2008JD010100.
Journel, A.G., Huijbregts, C.G., 1978. Mining Geostatistics. Academic, London, 600 pp.
Kahre, M.A., et al., 2011. Coupling Mars' dust and water cycles: Effects on dust lifting vigor, spatial extent and seasonality. In: Proceedings of the Fourth International Workshop on the Mars Atmosphere: Modelling and Observation, 8–11 February, Paris, France.
Kass, D.M., et al., 2014. Interannual Behavior of Large Regional Dust Storms, Eight International Conference on Mars, Pasadena (CA), USA, July 14–18. LPI Contribution No. 1791, p. 1169.
Kavulich Jr., M.J. et al., 2013. Local dynamics of baroclinic waves in the martian atmosphere. J. Atmos. Sci. 70 (11). http://dx.doi.org/10.1175/JAS-D-12-0262.1.
Kleinböhl, A. et al., 2009. Mars Climate Sounder limb profile retrieval of atmospheric temperature, pressure, and dust and water ice opacity. J. Geophys. Res. 114, E10006. http://dx.doi.org/10.1029/2009JE003358.
Kleinböhl, A. et al., 2011. A single-scattering approximation for infrared radiative transfer in limb geometry in the martian atmosphere. J. Quant. Spectrosc. Radiat. Transfer 112, 1568–1580.
Kleinböhl, A. et al., 2013. The semidiurnal tide in the middle atmosphere of Mars. Geophys. Res. Lett. 40 (10), 1952–1959.
Kuroda, T. et al., 2008. Semiannual oscillations in the atmosphere of Mars. Geophys. Res. Lett. 35 (23). http://dx.doi.org/10.1029/2008GL036061.
Heavens, N.G. et al., 2011. The vertical distribution of dust in the martian atmosphere during northern spring and summer: High-altitude tropical dust maximum at northern summer solstice. J. Geophys. Res. 116, E01007. http://dx.doi.org/10.1029/2010JE003692.
Lemmon, M.T. et al., 2004. Atmospheric imaging results from the Mars exploration rovers: Spirit and opportunity. Science 306, 1753–1756.
Lemmon, M.T., et al., 2008. The Phoenix surface stereo imager (SSI) investigation. Lunar Planet. Sci. 39. Abstract N. 2156.
Lemmon, M.T. et al., 2015. Dust aerosol, clouds, and the atmospheric optical depth record over 5 Mars years of the Mars Exploration Rover mission. Icarus 251, 96–111.
Lewis, S.R. et al., 2007. Assimilation of Thermal Emission Spectrometer atmospheric data during the Mars Global Surveyor aerobraking period. Icarus 192, 327–347.
Lorenc, A.C., Bell, R.S., MacPherson, B., 1991. The Meteorological Office analysis correction data assimilation scheme. Q.J.R. Meteorol. Soc. 117, 58–89.
Madeleine, J.-B. et al., 2011. Revisiting the radiative impact of dust on Mars using the LMD global climate model. J. Geophys. Res. 116, E11010. http://dx.doi.org/10.1029/2011JE003855.
Madeleine, J.-B. et al., 2012. The influence of radiatively active water ice clouds on the martian climate. Geophys. Res. Lett. 39, L23202. http://dx.doi.org/10.1092/2012GL053564.
Malin, M.C. et al., 2010. An overview of the 1985–2006 Mars Orbiter Camera science investigation. Mars 5, 1–60. http://dx.doi.org/10.1555/mars.2010.0001.
McCleese, D.J. et al., 2007. Mars Climate Sounder: An investigation of thermal and water vapor structure, dust and condensate distributions in the atmosphere, and energy balance of the polar regions. J. Geophys. Res. 112, E5. http://dx.doi.org/10.1029/2006JE002790.
McCleese, D.J. et al., 2010. Structure and dynamics of the martian lower and middle atmosphere as observed by the Mars Climate Sounder: Seasonal variations in zonal mean temperature, dust, and water ice aerosols. J. Geophys. Res. 115, E12016. http://dx.doi.org/10.1029/2010JE003677.
Millour, E., et al., 2011. An improved Mars climate database. In: Proceedings of the Fourth International Workshop on the Mars Atmosphere: Modelling and Observation, 8–11 February, Paris, France.
Millour, E., et al., 2014. A new Mars Climate Database v5.1, In: Proceedings of the Fifth International Workshop on the Mars Atmosphere: Modelling and Observation, 13–16 January, Oxford, UK.
Montabone, L. et al., 2006. Validation of martian meteorological data assimilation for MGS/TES using radio occultation measurements. Icarus 185, 113–132.
Montmessin, F. et al., 2004. Origin and role of water ice clouds in the martian water cycle as inferred from a general circulation model. J. Geophys. Res. 109 (E10).
Mulholland, D.P., 2012. martian Dust Lifting: Transport and Associated Processes, University of Oxford, D.Phil. Thesis.
Murchie, S. et al., 2007. Compact Reconnaissance Imaging Spectrometer for Mars (CRISM) on Mars Reconnaissance Orbiter (MRO). J. Geophys. Res. (Planets) 112 (E11), 5.
Navarro, T. et al., 2014. Detection of detached dust layers in the Martian atmosphere from their thermal signature using assimilation. Geophys. Res. Lett. 41, 6620–6626. http://dx.doi.org/10.1002/2014GL061377.
Pankine, A.A. et al., 2013. Retrievals of martian atmospheric opacities from MGS TES nighttime data. Icarus 226 (1), 708–722.
Piqueux, S. et al., 2015a. Variability of the martian seasonal CO_2 cap extent over eight Mars Years. Icarus 251, 164–180.
Piqueux, S. et al., 2015b. Enumeration of Mars years and seasons since the beginning of telescopic exploration. Icarus 251, 332–338.
Putzig, N.E., Mellon, M.T., 2007. Apparent thermal inertia and the surface heterogeneity of Mars. Icarus 191 (1), 68–94.
Read, P.L., et al., 2011. Midwinter suppression of baroclinic storm activity on Mars: Observations and models. In: Proceedings of the Fourth International Workshop on the Mars Atmosphere: Modelling and Observation, 8–11 February, Paris, France.
Sinnott, R.W., 1984. Virtues of the haversine. Sky & Telescope 68 (2), 159–161.
Smith, M.D., 2004. Interannual variability in TES atmospheric observations of Mars during 1999–2003. Icarus 167, 148–165.
Smith, M.D., 2008. Spacecraft observations of the martian atmosphere. Ann. Rev. Earth Planet. Sci. 36, 191–219.
Smith, M.D., 2009. THEMIS observations of Mars aerosol optical depth from 2002–2008. Icarus. http://dx.doi.org/10.1016/j.icarus.2009.03.027.
Smith, M.D. et al., 2003. Thermal Emission Imaging System (THEMIS) infrared observations of atmospheric dust and water ice cloud optical depth. J. Geophys. Res. 108, 5115. http://dx.doi.org/10.1029/2003JE002115.
Smith, M.D. et al., 2006. One martian year of atmospheric observations using MER Mini-TES. J. Geophys. Res. 111, E10. http://dx.doi.org/10.1029/2006JE002770.
Smith, P.H. et al., 2008. Introduction to special section on the Phoenix Mission: Landing site characterization experiments, mission overviews, and expected science. J. Geophys. Res. 113, E3. http://dx.doi.org/10.1029/2008JE003083.
Steele, L.J. et al., 2014a. The seasonal cycle of water vapour on Mars from assimilation of Thermal Emission Spectrometer data. Icarus 237, 97–115.
Steele, L.J., Lewis, S.R., Patel, M.R., 2014b. The radiative impact of water ice clouds from a reanalysis of Mars Climate Sounder data. Geophys. Res. Lett. http://dx.doi.org/10.1002/2014GL060235.
Vincendon, M. et al., 2009. Yearly and seasonal variations of low albedo surfaces on Mars in the OMEGA/MeX dataset: Constraints on aerosols properties and dust deposits. Icarus 200, 395–405.
Vincendon, M., et al., 2014. Mars Surface Albedo and Changes. ArXiv e-prints. 1407.2831v1.
Wang, H., 2007. Dust storms originating in the northern hemisphere during the third mapping year of Mars Global Surveyor. Icarus 189, 325–343.
Wang, H. et al., 2003. Cyclones, tides, and the origin of major dust storms on Mars. Geophys. Res. Lett. 30 (9), 1488. http://dx.doi.org/10.1029/2002GL016828.
Wang, H., Zurek, R.W., Richardson, M.I., 2005. The relationship between frontal dust storms and transient eddy activity in the northern hemisphere of Mars as observed by Mars Global Surveyor. J. Geophys. Res. 110 (E7), E07005. http://dx.doi.org/10.1029/2005JE002423.
Wang, H., Richardson, M.I., 2015. The origin, evolution, and trajectory of large dust storms on Mars during Mars years 24–30 (1999–2011). Icarus 251, 112–127.
Wilson, R.J., 2011. Dust cycle modeling with the GFDL Mars general circulation model. In: Proceedings of the Fourth International Workshop on the Mars Atmosphere: Modelling and Observation, 8–11 February, Paris, France, pp. 147–150.
Wilson, R.J., et al., 2008. Simulation of the 2001 planet-encircling dust storm with the NASA/NOAA Mars General Circulation Model. In: Proceedings of the Third International Workshop on the Mars Atmosphere: Modelling and Observation, 10–13 November, Williamsburg (VA), USA, No 1447, p. 9023.
Wilson, R.J., Noble, J., Greybush, S.J., 2011. The derivation of atmospheric opacity from surface temperature observations. In: Proceedings of the Fourth International Workshop on the Mars Atmosphere: Modelling and Observation, 8–11 February, Paris, France, pp. 116–119.
Wolff, R.T., Clancy, P.R., 2003. Constraints on the size of martian aerosols from Thermal Emission Spectrometer observations. J. Geophys. Res. 108, 5097. http://dx.doi.org/10.1029/2003JE002057.
Wolff, R.T. et al., 2006. Constraints on dust aerosols from the Mars Exploration Rovers using MGS overflights and Mini-TES. J. Geophys. Res. 111, E12S17. http://dx.doi.org/10.1029/2006JE002786.
Wolff, R.T. et al., 2009. Wavelength dependence of dust aerosol single scattering albedo as observed by the Compact Reconnaissance Imaging Spectrometer. J. Geophys. Res. 114, E00D04. http://dx.doi.org/10.1029/2009JE003350.